Nanoscale Advances

Accepted Manuscript

This article can be cited before page numbers have been issued, to do this please use: V. Shankar, E. Amutha, R. Subramanian, T. Madhumitha and G. Annadurai, *Nanoscale Adv.*, 2026, DOI: 10.1039/D5NA00783F.

ROYAL SOCIETY OF CHEMISTRY

rsc.li/nanoscale-advances

View Article Online
DOI: 10.1039/D5NA00783F

HIGHLY SELECTIVE HYDROGEN SENSOR AND SUPERCAPACITOR ELECTRODE MATERIALS FOR SnO_2-PANI NANOCOMPOSITES FOR EFFICIENT PHOTOCATALYST AND TOXICITY STUDIES IN ZEBRA FISH EMBRYOS

Amutha E[1], Rajaduraipandian S[2], Madhumitha T[1], Annadurai G[1]*

Dr. Amutha Eswaran [*1]; Dr. Rajaduraipandian Subramaniam[2]; Ms. Madhumitha Thirumalainambi [3], Dr. Gurusamy Annadurai *[4], Vijayalakshmi Shankar[*5]

[1] CSIR-Research Associate, SPKCEES, Manonmaniam Sundaranar University, Alwarkurichi – 627 412, India
[2]Sri Paramakalyani College, Manonmaniam Sundaranar University, Alwarkurichi - 627412, India
[3] Research Scholar, SPKCEES, Manonmaniam Sundaranar University, Alwarkurichi – 627 412, India
[4] Professor, SPKCEES, Manonmaniam Sundaranar University, Alwarkurichi – 627 412, India
[5]School of Healthcare Science and Engineering, Vellore Institute of Technology, Vellore – 14, India

***** *Corresponding author:* ***annananoteam@gmail.com****;* ***vijimicro21@gmail.com***

Abstract

Our current study presents the synthesis of binary hybrid Tin Oxide-Poly Aniline (SnO_2-PANI) nanocomposites, which have potential applications in gas sensing, energy storage, photocatalysis, and biomedicine. The ternary hybrid formation is confirmed by a number of characterization studies, including X-ray diffraction (XRD), Thermogravimetric Analysis (TGA), Particle Size Analyzer (PSA), Fourier transform infrared microscopy (FTIR), Scanning Electron Microscopy with Elemental Analysis (SEM-EDAX), Atomic Force Microscopy (AFM). The gas sensing capability of the nanoparticles showed good sensitivity for Hydrogen (H_2) at 50 ppm. The electrode material has a 94% sensing capacity and a 50-day stability period.The electrochemical performance of the binary hybrid is revealed by a three-electrode setup using a Potassium hydroxide (KOH) (3 M) electrolyte. The particles have a large surface area and a high current density, according to the electrochemical study. The bimetallic nanoparticle was used to degrade the Rhodamine dye in a photocatalytic chamber. 180 minutes later, the nanoparticles had removed 92% of the dye. The model animal showed only mild toxicity to the nanoparticles in the toxicity test, which was conducted to ascertain whether the photocatalyst was hazardous. The particles showed good activity against both Gram positive and Gram negative bacteria in the antibacterial test when compared to the control.

Keywords: Polymer, Nanocomposite, Energy storage, Sensor, Electrochemical studies and Biomedical Applications

View Article Online
DOI: 10.1039/D5NA00783F

1. Introduction

In recent times, inorganic-organic nanocomposites have become a very interesting field of study because of their distinct physical and chemical properties[1]. Tin oxide is a well-known substance that is utilized in gas sensors and dye-based solar cells due to its high band gap and n-type semiconductor nature[2]. Polyaniline has garnered attention because of its superior electrical conductivity, environmental stability, and ease of synthesis. One of SnO_2's advantages is that it's cheap and eco-friendly. It is crucial to develop and study composite materials that combine the benefits of SnO_2 and polyaniline (PANI) for electrochemical applications. Although SnO_2 exhibits promising sensing and electrochemical properties, its poor conductivity significantly restricts performance. Conducting polymers such as polyaniline (PANi) offer an effective strategy to mitigate these drawbacks by providing rapid charge transport pathways and flexible surface chemistry. Therefore, integrating SnO_2 with PANi can yield a synergistic composite with enhanced functional characteristics[3,4].

The conducting polymers have improved the gas detection capabilities, especially by lowering the operating temperature to about room temperature[5]. The conducting polymer polyaniline (PANI) has been studied as a potential material for gas sensing applications (or electroactivity) because of its intriguing redox chemistry, controlled electrical conductivity, and environmental stability[6]. PANI has garnered significant attention due to its significant features for H_2 gas detection at low operating temperatures, making it a useful conducting polymer[7].

The transition metal oxide hydrous ruthenium dioxide has been found to be one of the most promising options for electrode materials in electrochemical capacitors because of its many potential applications, including its capacity to reversibly store charges through redox reactions[8,9]. Nanoscale SnO_2 has been used as a promising gas sensor and electrode in batteries

View Article Online
DOI: 10.1039/D5NA00783F

made from lithium ion, solar cells with dye-sensitization, transparency conducting electrodes, electrochromic windows, displays with flat panels, catalytic supports, catalysts transistors, rechargeable batteries, and other applications[5,10,11]. It is commonly known that SnO_2 exhibits effective semiconductivity in addition to conventional redox properties, setting it apart from other, more conventional supports in catalytic applications[12].

In contrast, PANI-Tin oxide Nanocomposites enhance conductivity and thermal stability, making them ideal for flexible electronics and energy storage[13]. PANImetal oxide composites, such as those with TiO_2 or ZnO, boost photocatalytic activity and environmental stability, useful in sensors and anticorrosion coatings. PANI- Tin oxide Nanocomposites improve mechanical and barrier properties and are suitable for coatings and packaging[14].

It is still challenging for the SnO_2 photocatalyst's photocatalytic efficiency to meet the demands of practical use because of electron-hole pair recombination[15]. Improving photocatalytic performance is necessary to meet the demands of commercial applications[16]. The photocatalytic performance of the SnO_2 nanoparticles can be improved by changing the SnO_2 surface to generate smaller particles and a lower bandgap energy[17].

In this work, SnO_2–PANi nanocomposites were successfully synthesized through an in-situ polymerization approach. Comprehensive physicochemical analyses, including XRD, FTIR, SEM-EDX, AFM, TGA, and PSA, confirmed the crystalline structure, chemical interactions, elemental composition, surface morphology, thermal stability, and particle size distribution of the materials. The electrochemical performance of the synthesized nanocomposites was evaluated using cyclic voltammetry (CV), galvanostatic charge–discharge (GCD), and electrochemical impedance spectroscopy (EIS), demonstrating their suitability as high-performance electrode materials. Additionally, the nanocomposites exhibited notable

View Article Online
DOI: 10.1039/D5NA00783F

antimicrobial activity against selected bacterial strains, indicating their potential for multifunctional applications. Overall, the synergistic combination of SnO_2 and PANi enhances both electrochemical behavior and antimicrobial efficacy, suggesting that these nanocomposites may serve as promising candidates for advanced sensor technology and bio-protective applications.

2. Materials and Methods

Ammonium persulphate($(NH_4)_2S_2O_8$), anhydrous sodium carbonate(Na_2CO_3), tin chloride($SnCl_2$), sodium hydroxide(NaOH), and aniline ($C_6H_5NH_2$) ≥ 99.5% pure hydrochloric acid(HCL), nitric acid(HNO_3), sulfuric acid(H_2SO_4), and ethanol (C_2H_5OH) were purchased from Sigma-Aldrich. Every reagent that was bought was analytical grade, and it was all used without any additional purification. Aqueous solutions were prepared for each experiment using distilled water. The MTCC Chandigarh provided us with bacterial isolates of Gram-negative *Pseudomonas fluorescens*, *Enterobacter*, and Gram-positive Staphylococcus aureus.

2.1 Synthesis of tin oxide (SnO_2) nanoparticles

This method involved creating distinct solutions in distilled water of hydrated stannous chloride and anhydrous sodium carbonate. Stannous chloride solution and hydrated sodium carbonate solution are prepared in a 1:2 M ratio. Using a magnetic stirrer, the 1000 ml beaker containing the stannous chloride solution was continuously stirred at room temperature. A white precipitate was produced after five minutes of continuous stirring and drop-by-drop addition of sodium carbonate solution. Following thirty more minutes of stirring, the mixture was allowed to settle for four hours. The solution was first separated from the particles that had gathered at the bottom of the beaker by decantation, and then it was filtered. To get rid of the impurities, ethyl alcohol was used as a final wash for the precipitate. To produce SnO_2 nanoparticles, the

View Article Online
DOI: 10.1039/D5NA00783F

discovered product was dried for 12 hours at 60 °C and then calcined for 1 hour at 350 °C in a muffle furnace[18].

(i) Precipitation of tin hydroxide from $SnCl_4$ with NaOH:

$$SnCl_4+4NaOH\rightarrow Sn(OH)4\downarrow+4NaCl$$

(ii) Thermal dehydration / calcination of the hydroxide to SnO_2:

$$Sn(OH)_4\rightarrow SnO_2+2H_2O$$

(iii) Combine the two steps:

$$SnCl_4+4NaOH\rightarrow SnO_2+4NaCl+2H_2O$$

(iv) $SnCl_2$ and oxidize to SnO_2, an illustrative overall equation (with O_2 as oxidant) is:

$$SnCl_2+1/2O_2\rightarrow SnO_2+2Cl^-$$

2.2. Synthesis of Polyaniline (PANI)

Aniline was oxidized with ammonium per sulfate to form polyaniline. During this synthesis, a 0.5 M aniline solution in 0.5 M HCl is produced. Furthermore, 0.5M ammonium persulphate is dissolved in distilled water to make a solution. A magnetic stirrer is used to agitate the aniline hydrochloride solution in a 500 ml beaker for approximately ten minutes. Subsequently, 0.5 M ammonium per sulphate was progressively added to the solution while stirring continuously. Aniline hydrochloride's white solution progressively turns green. After stirring for thirty more minutes, the mixture was allowed to rest for two hours before being filtered. The result is a precipitate that is pale green and is referred to as polyaniline. Rinse the precipitate several times with distilled water to get rid of contaminants and unreacted aniline[18]. In the end, the precipitate was cleaned with acetone to get rid of the unreacted components. The finished product was dried for 12 hours at 50 °C. Using a mortar and pestle, the dried material was ground into a fine powder.

View Article Online
DOI: 10.1039/D5NA00783F

(i)Protonation: $C_6H_5NH_2 + HCl \rightarrow C_6H_5NH_3^+ + Cl^-$

(ii)Oxidation: $C_6H_5NH_3^+ + S_2O_8^{2-} \rightarrow [C_6H_5NH_2]^{\cdot+} + 2SO_4^{2-}$ (generation of aniline radical cation)

(iii) Coupling of radical cations → oligomers → chain growth → polyaniline (emeraldine salt).

2.3. Synthesis of SnO_2-PANI Nanocomposites

A 500 ml beaker was filled with a dissolved aniline solution in Hydrochloric acid, and it was agitated for five minutes. After that, 0.5 g (10 wt%) of SnO_2 nanoparticles were added, and a magnetic stirrer was used to agitate the mixture for around 15 minutes. After stirring for an additional ten minutes and adding ammonium per sulphate drop by drop, the precipitate was left to settle for thirty to 40 minutes. To get rid of the contaminants, the precipitous was filtered in addition then repeatedly cleaned with purified water. Following acetone cleaning besides a 24-hour drying process at 50 °C, the precipitate was then pulverized.

2.4. Electrochemical Measurement

The working electrode (WE) made of Ni foam had an exposed geometric area of 1 cm². The Ni foam was cut into pieces of 1 cm × 1 cm, thoroughly cleaned, and used as the substrate for electrode fabrication. The electrochemical behavior of SnO_2-PANI nanocomposites was examined using cyclic voltammetry (CV), galvanostatic charge-discharge (CD), and electrochemical impedance spectroscopy (EIS). The working electrode was made by combining the nanocomposite materials in an 85:15:10 weight ratio with the conductive carbon (Carbon Black) and binder PTFE (Polytetrafluoroethylene). The resultant electrode paste (~2 mg) was applied to a Ni foam current collector that had already been prepared in order to use it as a working electrode. Electrochemical studies were performed in a 3 M Potassium Hydroxide electrolyte using a three-electrode cell, where Ag/AgCl was the reference electrode and Pt foil was the counter electrode. Different scan and current rates were employed in CV and CD

View Article Online
DOI: 10.1039/D5NA00783F

investigations.The discharge profile was utilized to compute the specific capacitance, energy density, and power density of the system through the application of the subsequent formula:

$$C_{sp} = \frac{\int IdV}{mv\Delta V} \quad (1)$$

$$C_{sp} = \frac{I\Delta t}{m\Delta V} \quad (2)$$

where "M" is the mass of active material, "S" is the scan rate, "∫ IdV" is the absolute surface area, and "ΔV" is V_2 - V_1 = Potential window.

The energy density (E) and power density (P) were calculated based on the electrochemical data obtained from galvanostatic charge–discharge (GCD) measurements. Specifically:

(i) The energy density (E) was calculated using the discharge time (Δt) obtained from the GCD curve and the specific capacitance (C) determined in the three-electrode setup, as expressed in Equation 2:

$E=1/2\ CV^2$ ----------(1)

where *V* is the operating potential window.

(ii) The power density (P) was subsequently calculated using the discharge time and energy density values:

$P=E/\Delta t$ ---------- (2)

2.5. Fabrication of Gas sensing electrode

The active substrate for the fabrication of gas sensing electrodes was printed circuit boards (PCB). The PCB's conducting layer had to be cleaned before a 1 cm2 area could be taken and drawn with positive resist to prepare the contact channel. Next, dipping into the $FeCl_3$ solution was used to complete the etching procedure. To remove the resist substance, acetone

View Article Online
DOI: 10.1039/D5NA00783F

was utilized. Using a spin coater set to 4000 rpm for 5 minutes, the substrate was finally covered with the sensing material (SnO_2-PANI nanocomposites). The electrodes were dried for thirty minutes at 80 ºC in a vacuum oven. In order to connect the single core wires to the voltage source for sensor measurements, they were linked at the terminals.

2.6. Antibacterial Property

2.6.1. Agar Well Diffusion Assay

Gram-positive Staphylococcus aureus, Gram-negative Enterobacter, and Pseudomonas fluorescens were used as pathogenic bacteria in the well diffusion method to examine the SnO_2-PANI nanocomposites' antibacterial activity. In order to determine the antibiotic activity of the aforementioned bacterial species, various concentrations of 25, 50, 75, and 100 µl were used. The zone of bacterial inhibition was found after each plate was treated for 24 hours at 37°C.

2.7. Photocatalytic activity

The photocatalytic performance of SnO_2-PANI nanocomposites was evaluated by measuring the photocatalytic degradation of Rhodamine dye under UV irradiation. A standard procedure involved adding 0.1 g to 100 mL of an aqueous Rhodamine dye solution with a starting concentration of 1 ppm. To achieve adsorption/desorption equilibrium, the SnO_2-PANI nanocomposites suspension and dye solution were shaken for thirty minutes in the dark before exposure to radiation. After then, the suspension was subjected to UV light. At regular intervals of thirty minutes, about two milliliters of the suspension were taken out of the mixture and centrifuged to separate the photocatalyst particles during irradiation. A UV-vis spectrophotometer was used to quantify the concentration of Rhodamine solution in the supernatant. This instrument has a unique absorbance at $\lambda max = 550$ nm.

The following formula was used to determine the deterioration efficiency:

View Article Online
DOI: 10.1039/D5NA00783F

$$Degradation\ efficiency = \frac{C_o - C}{C_o} \times 100\%$$

Where Co is the starting concentration of rhodamine dye and C is the concentration of the rhodamine dye solution following the "t" degradation time.

2.8. Fish maintenance and SnO_2-PANI nanocomposites exposure

Wild zebrafish (Danio rerio) had been collected by the Fisheries Department in Madurai, India. For a month, the fish were acclimated in the zebrafish tank at SPKCEES, Manonmaniam Sundaranar University in Alwarkurichi, India. The glass aquarium held a 50-liter capacity and was kept at a constant temperature of about 28 °C with a light-dark cycle of 14:10 hours (6.8-8.5). Fish were fed live Artemia nauplii from Inve Aquaculture Nutrition in Thailand once a day and commercial dry flakes food called Basic Flake from China twice a day. A single female zebrafish and two male zebrafish in a single breeding tank were mated to produce embryos. To facilitate reproduction, males and females were physically separated from one another at the same time of day by a clear block. This barrier was then removed the next morning. To get rid of any remaining material from their surface, the eggs were rinsed several times in the E3 medium. Twenty embryos in 2 milliliters of solution per well were added right away to the fertilized eggs in the 6, 12, 24, and 48-well culture plates. Every experimental treatment and control group was duplicated three times. SnO_2-PANI nanocomposites at various concentrations (0, 25, 50, 75, 100, 250 μg/ml) were cultivated in healthy fertilized embryos for 24 to 96 hours post fertilization. Every 24 hours, groups exposed to SnO_2-PANI nanocomposites had their dead embryos removed from the plates. Every experimental plate was covered with foil and maintained at 28°C to keep light from penetrating.

2.9. Embryo Toxicity test

View Article Online
DOI: 10.1039/D5NA00783F

Using a stereomicroscope, the zebrafish embryo's embryonic developmental stage was examined during the whole exposure time after fertilization. The embryos were exposed to different doses of SnO_2-PANI nanocomposites (0, 25, 50, 100, and 200 µg/ml) for a period of 24-96 hpf. The rate of hatching and the rate of embryonic death were measured each 24 hours. The term "hatching rate" refers to the proportion of viable embryos left in each well after hatching. Photographs and documentation of the deformities in the embryos and larvae from the treatment and control groups were taken. The malformed embryos were imaged using a stereomicroscope, and the percentage of malformed embryos was recorded every 24 hours.

3. Results and Discussion

3.1. UV-Vis Absorption Spectroscopy & Bandgap Measurement

The UV–Vis study was carried out to determine the optical band gap and to understand the optical behavior of the synthesized materials. The UV-vis absorbance spectra of SnO_2-PANI, Polyaniline, and tin oxide nanocomposites materials are displayed in Figure 1. The synthesized materials exhibit a clear absorption of visible and ultraviolet light. The tin oxide light absorbance peak, located at 298 nm in the UV range, is attributed to the $\pi \rightarrow \pi^*$ transition of C–C bonds, while the poly aniline peak, located at 296 nm, signifies the $n \rightarrow \pi^*$ transition, as shown in Figure 1. The tauc plot inset inside each graph was used to calculate the estimated band gaps of 2.3 eV (SnO_2) and 4.02 eV(PANI)[19]. The SnO2-PANI nanocomposites exhibit UV absorption signals with a band edge of 288 nm and a high absorption intensity of 228 nm, with a corresponding bandgap of 3.4 eV. When compared to their individual spectra, the composite particle signals exhibit strong coupling reactions that are indicated by the red shifts in the peaks and also

View Article Online
DOI: 10.1039/D5NA00783F

connected to the quantum confinement or quantum size effects [20]. Additionally, the materials' bandgap is significantly changed when polyaniline is incorporated [21].

The optical band gap was calculated using the Tauc relation,

$$(\alpha h\nu)^n = A\,(h\nu - E_g)$$

where α is the absorption coefficient, $h\nu$ is the photon energy, A is a constant, E_g is the optical band gap, and n depends on the nature of the electronic transition (for direct allowed transition, $n = 2$).

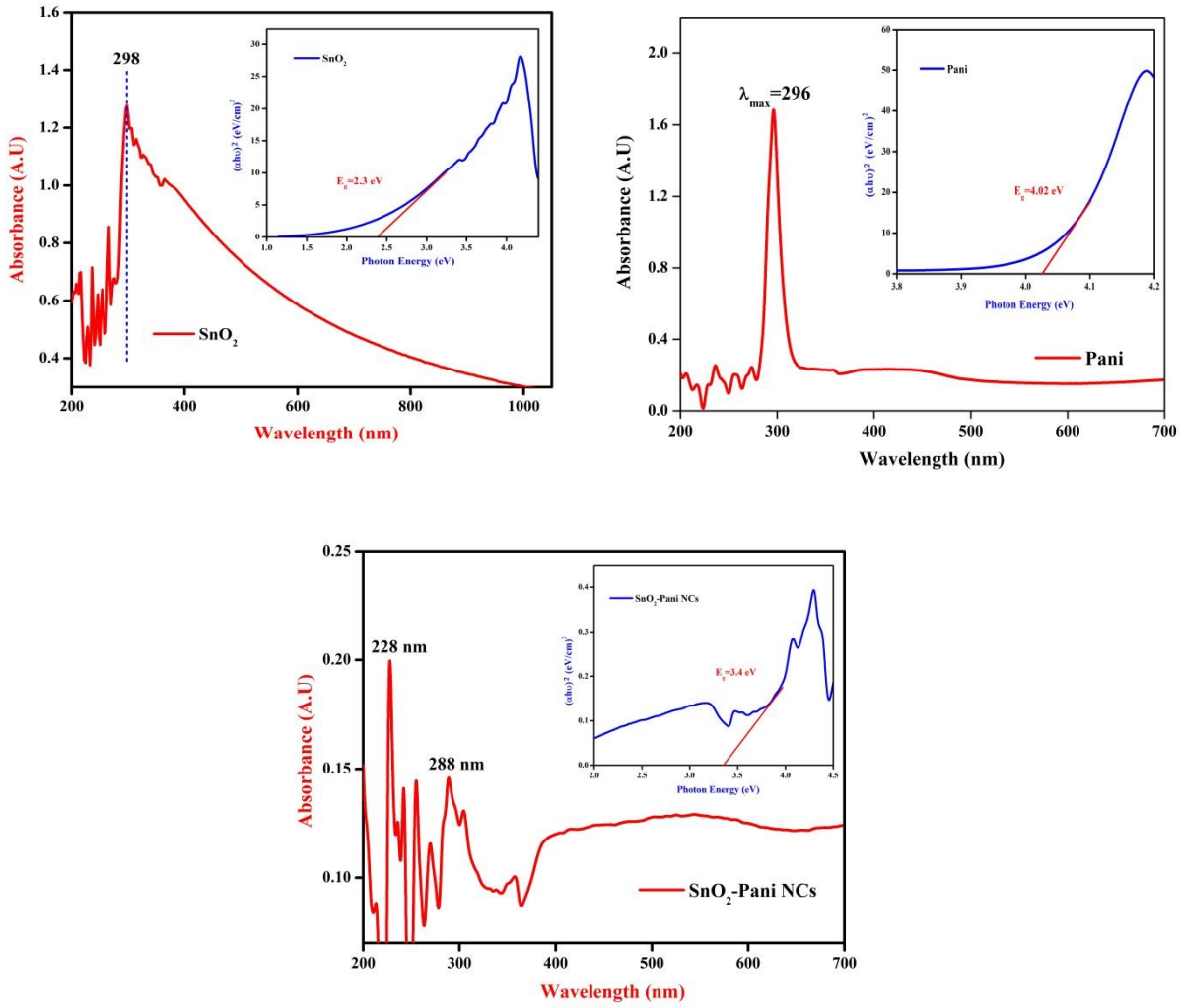

Fig. 1 UV Vis spectrum and Tauc Plot of (a) tin oxide, (b) polyaniline and (c) SnO_2-PANI nanocomposites

3.2. Fourier Transform Infrared Spectroscopy

View Article Online
DOI: 10.1039/D5NA00783F

Figure 2 shows a plot of the synthesized materials' FTIR spectra. It was determined which functional groups interacted with the metal oxide atoms in polyaniline. The OH, C=C, and C-X groups are primarily responsible for the peak seen in the FTIR spectra of tin oxide, which is located at 3355 cm^{-1}, 1640 cm^{-1}, and 502 cm^{-1}. For PANI-SnO_2 nanocomposites, the OH group's stretching mode is responsible for the strong absorption peak at 3355 cm^{-1}. The C=C, C–H, C–N, C–Br, and C–Br stretching modes are responsible for peaks at 1640 cm^{-1}, 1494 cm^{-1}, 1286 cm^{-1}, 476 cm^{-1}, and 442 cm^{-1}, respectively[22]. The interatomic vibrations produced the stretching band of polyaniline, which was detected at 2575 cm^{-1}.

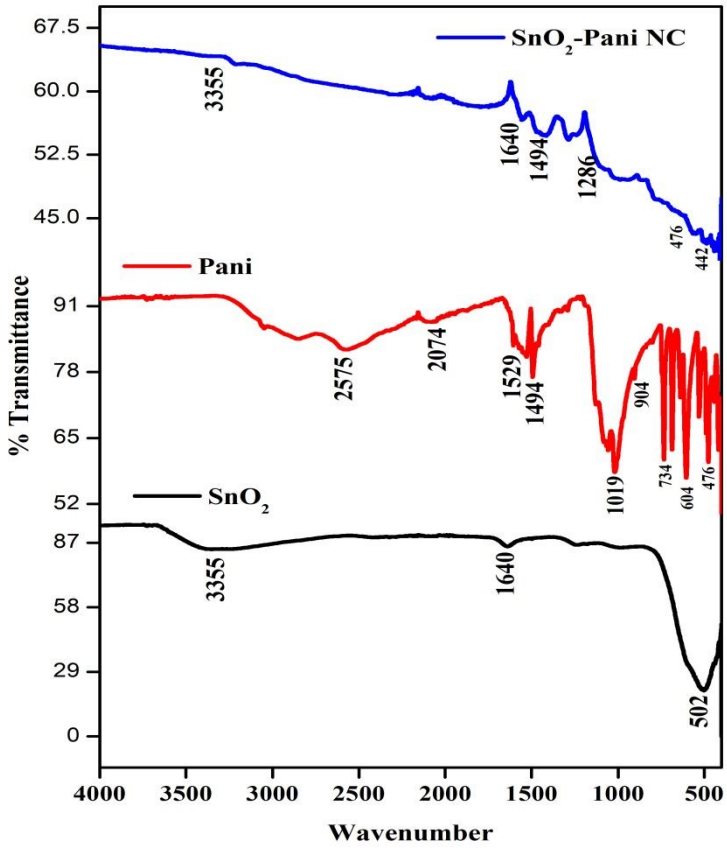

Fig. 2 FT-IR spectrum of (a) tin oxide, (b) polyaniline and (c) SnO_2-PANI nanocomposites

The following four peaks: 1529 cm^{-1}, 1494 cm^{-1}, 1019 cm^{-1}, 904 cm^{-1}, 734 cm^{-1}, 604 cm^{-1}, and 476 cm^{-1} correspond to the following characteristics: –C=C–, C–H, C–N, C-C, C–Br, C–

View Article Online
DOI: 10.1039/D5NA00783F

H, and C–X. The transmittance levels of the samples were increased in all of the samples when compared to the FTIR spectrum of tin oxide, Polyaniline, and SnO_2-PANI nanocomposites. This indicates that the bonding properties of the PANI-SnO_2 nanocomposites are affected by the reduction of the nanocomposites and the incorporation of metal oxide[23]. The presence of dopants in the mixed nanocomposite results in peaks shifting both downward and upward, which is related to the binding of the functional groups of SnO_2-PANI nanocomposites with the metal oxides [24].

3.3. Structural analysis

Through powder X-ray diffraction, phase purity and crystallographic data were obtained for the SnO_2 and SnO_2 modified by polyaniline nanocomposites. XRD patterns for PANI, SnO_2-PANI, and tin oxide nanocomposites are displayed in Fig. 3(a-c), in that order.

View Article Online
DOI: 10.1039/D5NA00783F

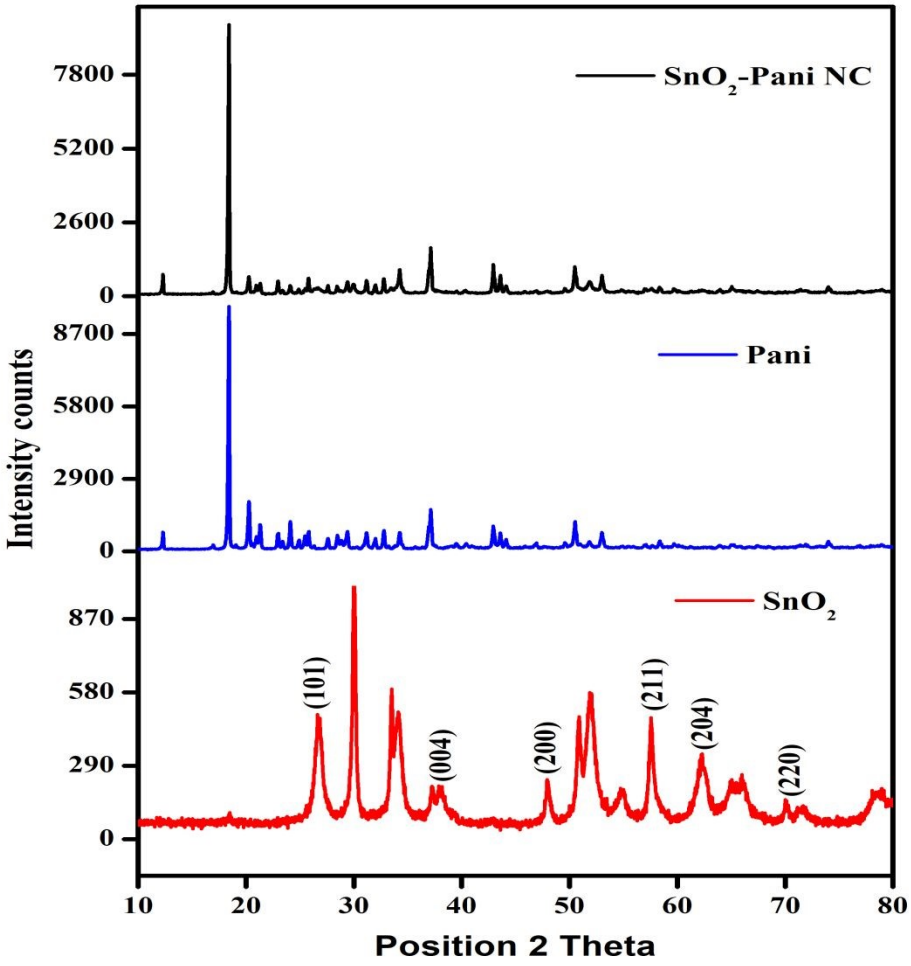

Fig. 3 XRD patterns for (a) tin oxide, (b) polyaniline and (c) SnO_2-PANI nanocomposites

Diffraction peaks were visible along (101), (004), (200), (211), (204), and (220) in the XRD pattern of tin oxide nanoparticles. Three broad peaks can be seen in the XRD pattern of Poly Aniline at 2θ values of 18º, 20º, 35º, and 50º, which suggests that the substance is amorphous. When the observed XRD peaks for the two samples are compared, it is evident that the peaks along (101), (004), (200), (211), and (220) with primitive tetragonal structure are matched with the observed nanocrystalline SnO_2 peaks (JCPDS DATA CARD 41-1445)[25]. The PANI matrix, however, may be the reason for these peaks' slight displacement from their

View Article Online
DOI: 10.1039/D5NA00783F

respective standard positions [7]. Additionally, in comparison to the XRD of pure SnO_2, we saw less intense peaks and comparatively more peak broadening.

3.4. Surface morphological analysis

Figure 4(a-c) displays the SEM micrographs of the SnO_2-PANI nanocomposites, polyaniline, and tin oxide, respectively. The SEM image of SnO_2 nanoparticles produced by the co-precipitation method is shown in Figure 4(a). The particles have a spherical shape and are uniformly distributed, with sizes less than 100 nm. It is possible that the larger particles in this figure are collections of the smaller ones. [6] found that the tin particle size decreased as pH increased from 6 to 9, but that it did not change after that. Regarding the Polyaniline particles (Fig. 4(b)), the particle growth seems to be spherical in shape, with a diameter ranging from 50 to 100 nm. The composite particles in PANI- SnO_2 nanocomposites exhibit high dispersion and agglomeration (see Figure 4(c)). It seems highly likely that the nanostructured SnO_2 particles are embedded within PANI chains based on the SEM images[26].

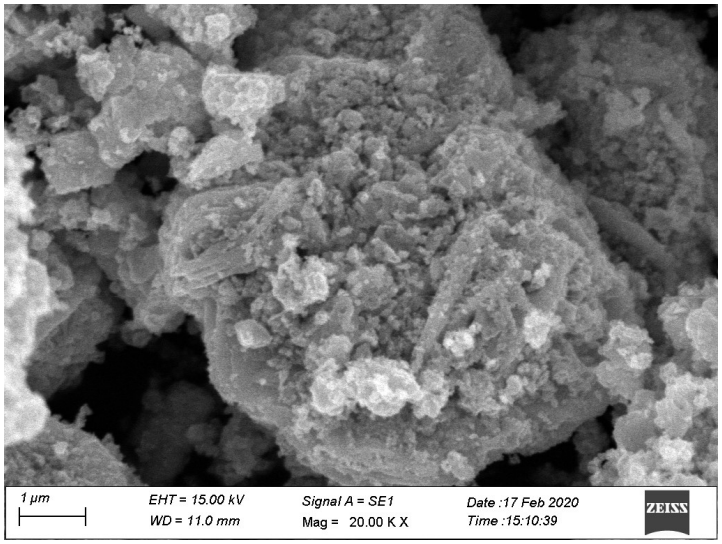

Fig. 4. (a) SEM micrographs for tin oxide

View Article Online
DOI: 10.1039/D5NA00783F

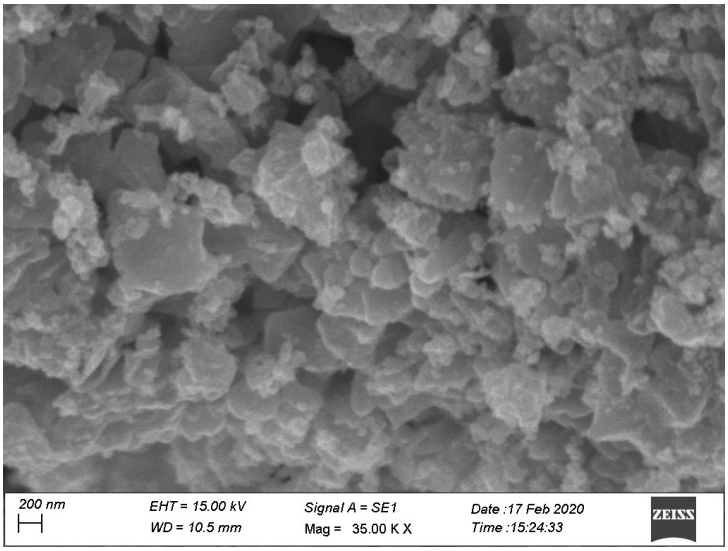

Fig. 4. (b) SEM micrographs for polyaniline

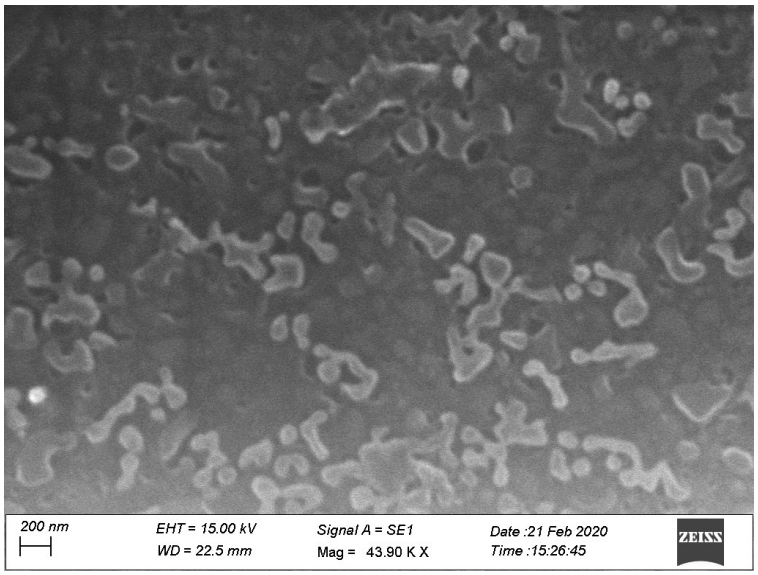

Fig. 4. (c) SEM micrographs for SnO_2-PANI nanocomposites

View Article Online
DOI: 10.1039/D5NA00783F

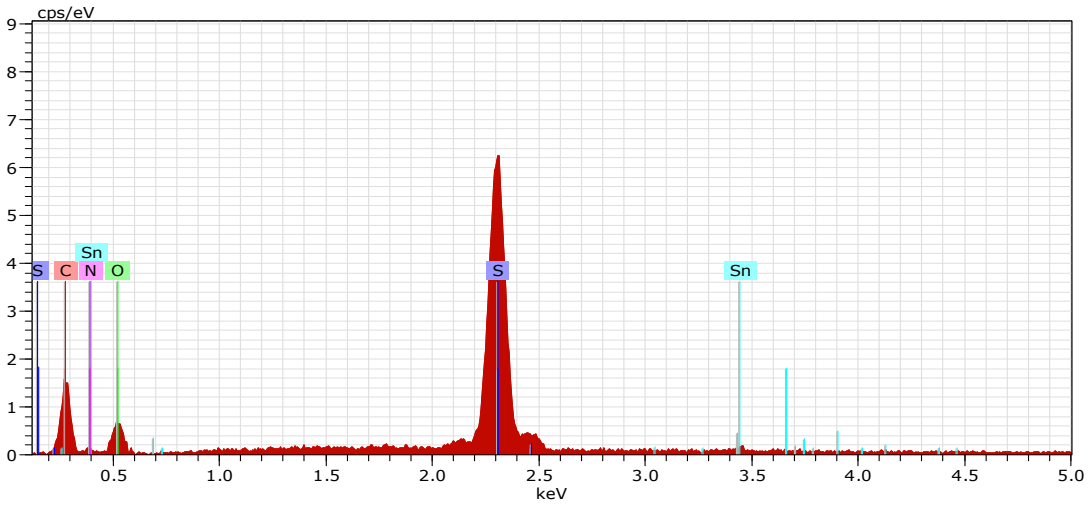

Fig. 4 (D) Edax spectrum of SnO_2-PANI nanocomposites

The SnO_2-PANI nanocomposites' EDX spectrum (figure 4(D)) shows that the only components present are tin, sulfur, nitrogen, and oxygen. There was no evidence of contamination with sodium or chlorine in the product. According to the quantitative SEM EDX analysis, the percentage of oxygen is roughly 40.79%, whereas the percentages of tin and sulfur are roughly 20.58 and 25.63%. The observation of nearly twice as much oxygen as tin, nitrogen, and sulfur confirms the chemical composition of PANI-SnO2 nanocomposites[27].

3.5. Thermo Gravimetric Analysis:

Figures 5, 6, and 7 illustrate the TGA analysis of the dried tin oxide, polyaniline, and SnO_2-PANI nanocomposites at optimal concentration. The samples were aged for 24 hours in air and then heated at a rate of 20 °C min-1 in a nitrogen atmosphere between 20 and 800 °C. In SnO2, the corresponding initial weight loss was 17.73 mg in the 50–80 °C temperature range. Up to 600 °C, the SnO_2 nanoparticles remained thermally stable and did not break down. There were two phases in the weight reduction from polyaniline [28]. The initial decrease in temperature was between 185 and 264 °C, which could be explained by the PANI's water evaporating. The second weight loss, which ranges from 344 to 406 °C, is related to ammonium per sulfate breaking

View Article Online
DOI: 10.1039/D5NA00783F

down. a significant weight loss of -10.11 mg in SnO_2 modified by polyaniline at temperatures between 169 and 268 °C. The evaporation of water from the metal oxides is responsible for this initial weight loss. The second weight loss in SnO_2 modified with polyaniline ranged from 328 to 490 °C. Decomposition of ammonium per sulphate in SnO_2 and polyaniline-modified SnO_2 to ammonium per sulphate and polyaniline is responsible for this second weight loss. The PANI-SnO_2 composite decomposes slowly from 169 to 490 °C, while PANI breaks down between 185 and 406 °C. This suggests that PANI had a strong interaction with the SnO_2 surface, improving polyaniline's thermal stability [29].

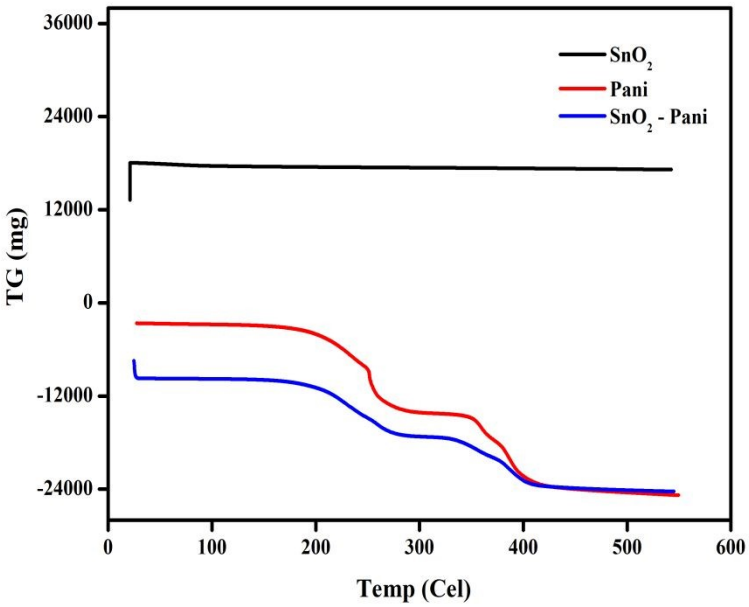

Fig. 5. TG curves of (a) tin oxide, (b) polyaniline and (c) SnO_2-PANI nanocomposites

View Article Online
DOI: 10.1039/D5NA00783F

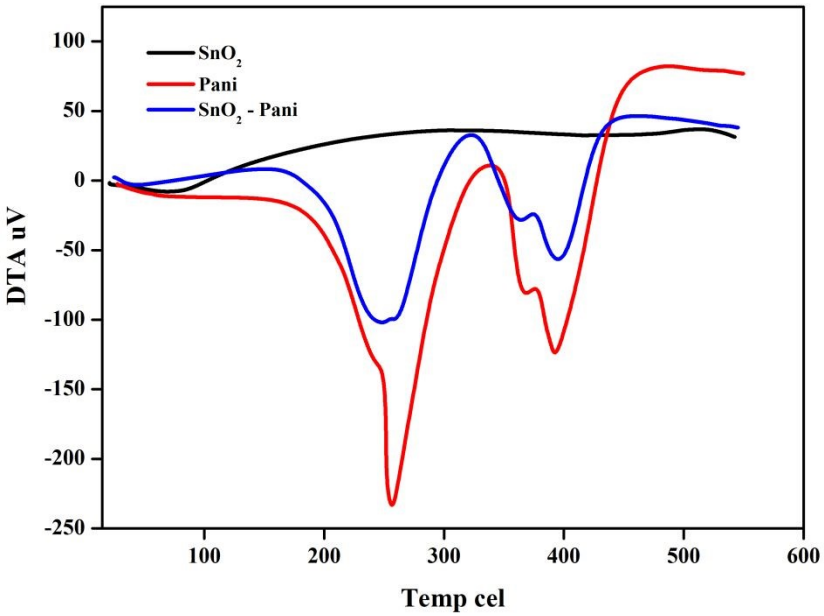

Fig. 6 DTA curves of (a) tin oxide, (b) polyaniline and (c) SnO_2-PANI nanocomposites

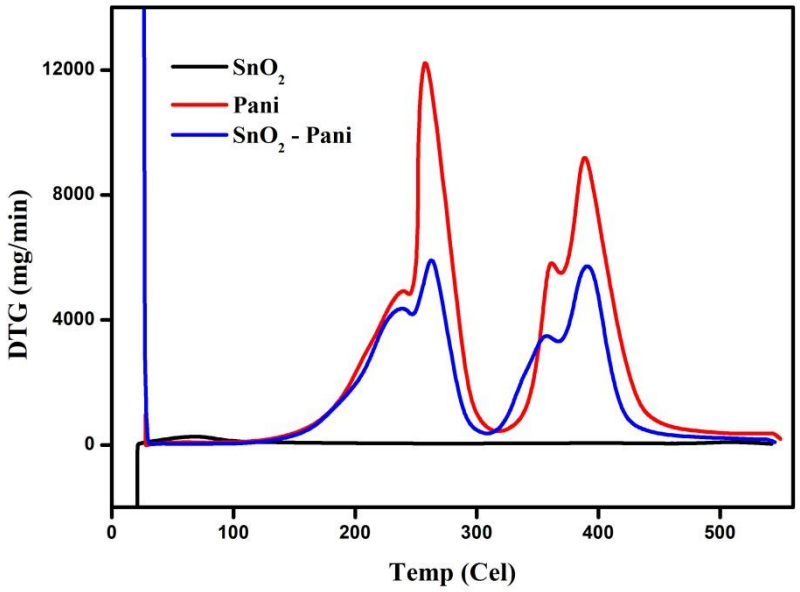

Fig. 7 DTG curves of (a) tin oxide, (b) polyaniline and (c) SnO_2-PANI nanocomposites

3.6. DLS Particle size analyzer

View Article Online
DOI: 10.1039/D5NA00783F

Dynamic Light Scattering (DLS) was used to measure the size distribution of the SnO_2-PANI, polyaniline, and tin oxide nanocomposites. DLS examines how Brownian motion causes particles to move in a solution. The majority of the particle sizes in a sample are used to calculate the average size. The charge ratio and size reduction have no relationship, but the polydispersed index does describe the homogeneity of the loaded particles; the lower the index, the more uniform the particles. Using a solution of nanoparticles, the DLS method measures the intensity of scattered light[30]. According to an analysis of the dynamic light scattering (DLS) data, tin oxide nanoparticles with an average diameter of about 100 nm form in the solution with a standard composition (Figure 8(a)). The average size distribution of polyaniline is 80–100 nm, as shown in Fig. 8(b). Similarly, figure 8(c) of Tin Oxide/Polyaniline illustrates the average size ranges between 70-100 nm. A high-resolution, multimodal deconvolution analysis that is proprietary was used for the statistical analysis in order to accurately measure the diameter of the nanoparticle.

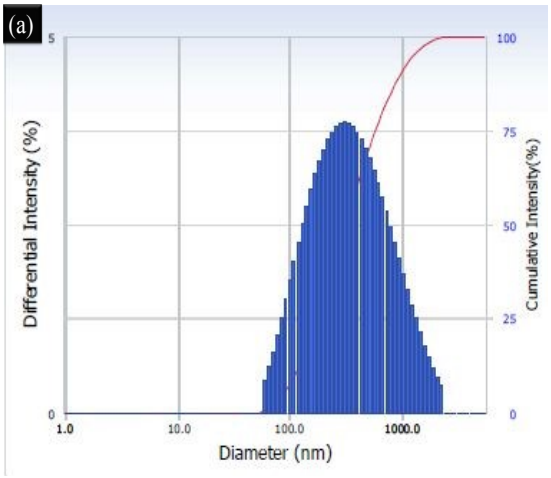

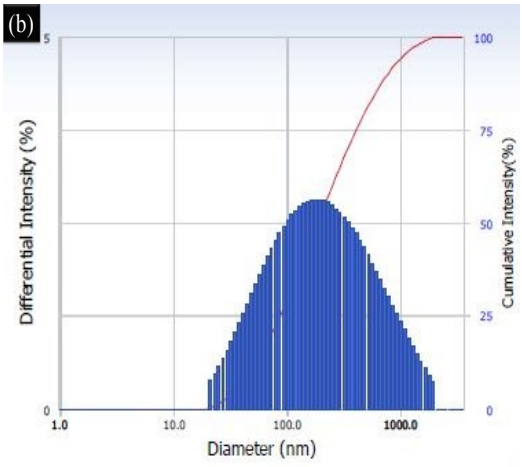

View Article Online
DOI: 10.1039/D5NA00783F

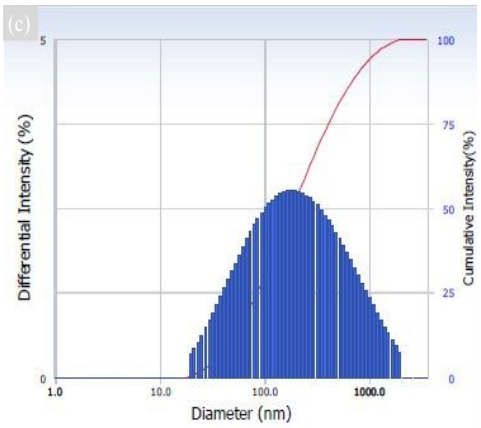

Fig. 8 DLS Particle size analyzer for (a) tin oxide, (b) polyaniline and (c) SnO_2-PANI nanocomposites

3.7. Atomic force microscopy

Figure 9(a) displays the SnO_2-PANI AFM image. The maximum grain height and maximum grain width for these nanolayers were estimated, according to the exact standard AFM depth. It was evident from the image that PANI had been deposited on SnO layers. Additionally, the PANI deposition had no effect on the SnO's surface area [31].

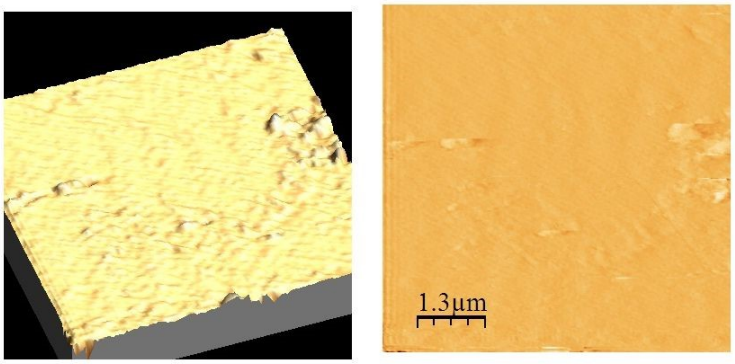

Fig. 9 (a) AFM micrographs for SnO_2-PANI nanocomposites

In Figure 9(b), the AFM image of PANI at 310 nm is displayed. The AFM image shows aggregated grains and a uniform distribution of polyaniline across the surface. [32] obtained distinct grain with distinct PANI boundaries.

View Article Online
DOI: 10.1039/D5NA00783F

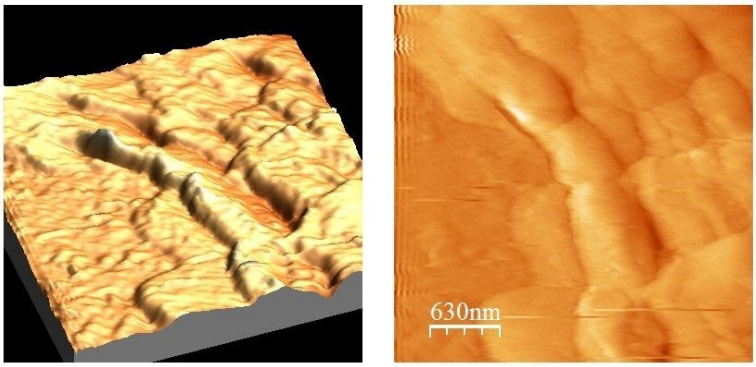

Fig. 9(b) AFM micrographs for polyaniline

Figure 9(c) shows AFM images of nanocrystalline films of tin oxide. The polycrystalline structure with well-shaped grains is visible in the AFM image. Due to the presence of SnO, the surface appears rough. As a result, the SnO particles' adsorption capacity is increased.

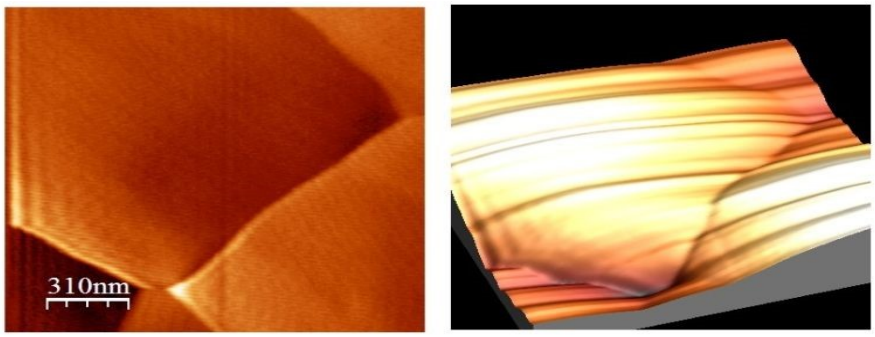

Fig. 9(c) AFM micrographs for tin oxide

3.8. Gas Selectivity Test

The material used in a practical gas sensing electrode should be able to react actively to a specific gas only. The current study assessed the materials' selectivity by introducing 50 parts per million of different target gases, including NH_3, CO_2, H_2, O_2, and LPG. Figure 10 shows a bar chart plotting the sensitivity values. For accuracy, the selectivity was measured independently three times, and the resulting values were plotted as error bars [33]. The electrode composed of

View Article Online
DOI: 10.1039/D5NA00783F

SnO_2-Poly aniline nanocomposite exhibits a greater response to H_2 than the other pristine and mixed composites, as can be seen in the figure. For the SnO_2-Poly aniline Nanocomposite to have high selectivity towards H_2, it is essential.

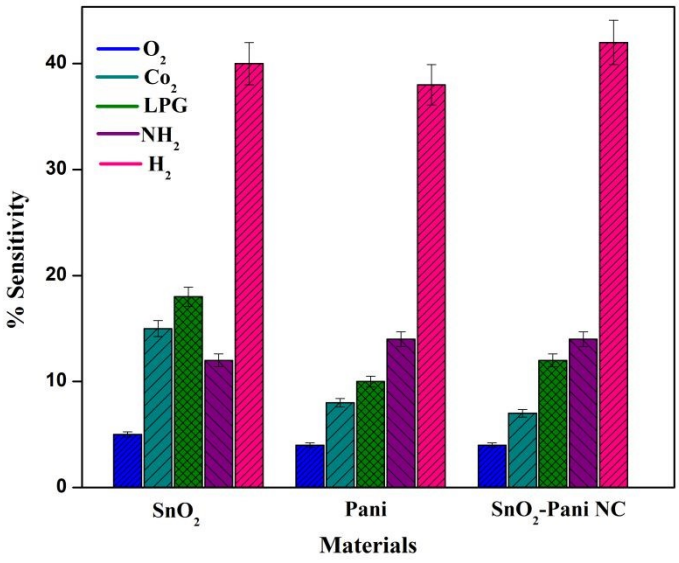

Fig. 10 Selectivity test towards various analyte gases of SnO_2, Pani and SnO_2- Pani Nanocomposite

The high selectivity of the synthesized materials, including the nanocomposite (NC), toward H_2 gas can be attributed to the strong interaction between hydrogen molecules and the surface-active sites of the SnO_2–PANI composite. Hydrogen has a smaller molecular size and higher diffusivity, which allows it to easily reach and react with the adsorbed oxygen species on the sensor surface. This reaction leads to a more significant change in resistance compared to other test gases.

Moreover, the presence of PANI in the composite enhances the surface adsorption capacity and facilitates charge transfer at the SnO_2–PANI interface, further improving sensitivity

View Article Online
DOI: 10.1039/D5NA00783F

and selectivity toward H_2. These factors collectively contribute to the observed selective response.

3.8.1. Gas Sensitivity Test

An alternative method for resolving sensitivity and selectivity problems as well as for modern, efficient room temperature operation is the fabrication of metal oxide nanocomposite. The sensing parameters of the prepared materials were analysed using a Keithley 6487 picoammeter/voltage source. The following formula was used to determine the electrodes' sensing response to H_2 and other analyte gases, such as CO_2, LPG, and NH_2.

$$\% S = \frac{Rgas - Rair\ (\Delta R)}{Rair\ (Ra)} * 100\ \%$$

In this case, the resistance of the electrode in the presence of air and analyte gas is represented by R_{air} and R_{gas}, respectively. Figure 11 shows the response of the different prepared electrodes to 50 ppm of H_2 at 40% relative humidity. Finding the material composition that exhibits the highest sensitivity to H_2 was the goal of the current study. An important factor in the sensing response is the atoms on the surface of the electrode material's grain boundary. Because of its high electron mobility, the SnO_2-Poly aniline Nanocomposite is crucial for room temperature sensing in this situation. One of the key parameters for assessing the material's performance for gas sensing was the sensor's response and recovery time [34]. The time required to apply input gas

View Article Online
DOI: 10.1039/D5NA00783F

on and gas off while achieving 90% of the maximum resistance change is known as the response and recovery time. Response value as resistance decreased for SnO_2-Poly aniline nanocomposite when H_2 was present at a concentration of 50 ppm. Tab 2 contains a tabulation of the observed response recovery and percentage sensitivity values. The sensing electrode has been exposed to concentrations ranging from 5 to 70 ppm, and the corresponding graph is shown in Figure 11.

Table 2 Comparison of the parameters of the electrodes towards Hydrogen sensitivity

Materials	**Response (%Sensitivity)**	**Response time (sec)**	**Recovery time (sec)**
SnO_2	27	53	117
Poly aniline	6	91	-
SnO_2-Poly aniline Nanocomposite	7	44	-

View Article Online
DOI: 10.1039/D5NA00783F

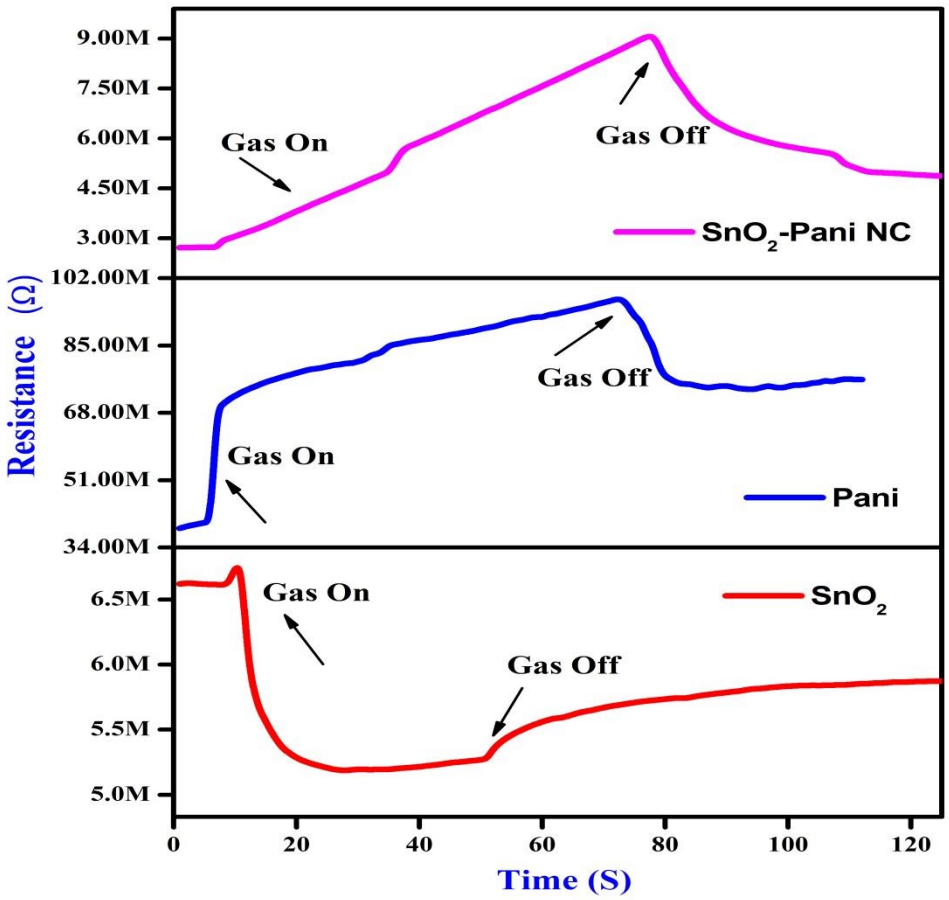

Fig. 11 50 ppm ammonia sensing response values of SnO_2-Poly aniline Nanocomposite

3.8.2. Electrode Stability Test

The sensing electrodes' ability to consistently reproduce the response value over an extended period of time is known as stability. Here, a 50-day test was conducted with 10-day intervals to evaluate the electrodes' stability. Figure 12 shows the plotted responses that were recorded. SnO_2-Poly aniline Nanocomposite electrodes preserved 94% of the sensing values, respectively[35]. Because the electrodes are operating at room temperature, the stability results show that the electrodes produce improved stability over a 50-day period. The SnO_2-Poly aniline Nanocomposite exhibited the highest stability response when the sensing electrodes were tested.

View Article Online
DOI: 10.1039/D5NA00783F

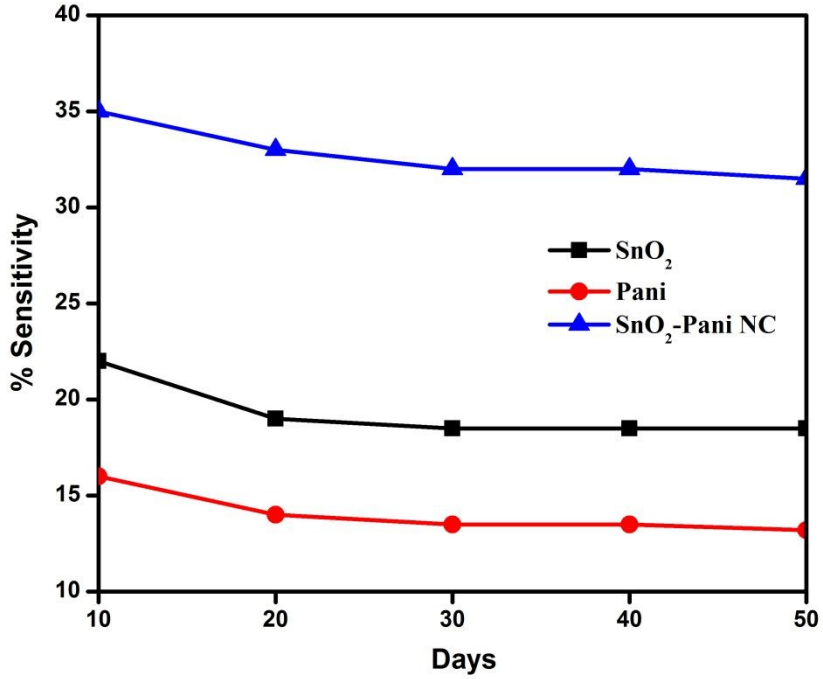

Fig. 12 Stability of the sensing electrode towards H_2 for the period of 50 days

3.8.3. Gas Sensing Mechanism

The sensing mechanism of metal oxide gas sensors must be understood in order to design and fabricate novel materials that perform exceptionally well for gas sensing. The gas response is primarily caused by the trapping of electrons at adsorbed molecules and band bending induced by these charged molecules, although the precise fundamental mechanisms causing this change in conductivity are still up for debate [36]. This article provides a brief overview of the n-type metal oxide sensing mechanism in air using SnO_2 as an example. The SnO_2 sensing material's surface usually absorbs oxygen gases when exposed to air. From the interior of the SnO_2 film, the adsorbed oxygen species can extract electrons. Reduced conductivity results from a depletion layer created by the negative charge trapped in these oxygen species. Reduced potential barrier height and increased conductivity are the results of the oxygen adsorbate's ability to trap

View Article Online
DOI: 10.1039/D5NA00783F

electrons, which return to the SnO_2 film when the sensor is exposed to reducing gases. The surface contains a variety of oxygen species, ranging from atomic (O^-, O_2^-) to molecular (O_2^-) ions, depending on the operating temperature [37]. In general, the molecular form predominates below 150 °C, whereas atomic species are found above this temperature.

The surface conductivity of the metal oxides is largely determined by the total surface stoichiometry. Adsorbed oxygen ions function as surface acceptors, binding elections and reducing surface conductivity, whereas oxygen vacancies act as donors, raising the surface conductivity. The energy diagram of different gas-phase oxygen species bound to the SnO_2 lattice and adsorbed at its surface is depicted in Figure 13. As the temperature rises, the reaction O_2 − ads + e− = 2O− ads occurs on SnO_2 films. For O− ads ions, the desorption temperatures from the SnO_2 surface are approximately 550 °C, while for O_2− ads ions, they are approximately 150 °C. Band bending and surface conductivity change in tandem with the transition, which results in an increase in surface charge density at constant oxygen coverage.

Measurements of conductance indicate that the transition occurs gradually. Consequently, a steady and gradual change in the conductance usually occurs after a sudden change in the sensors' temperature [38]. As the oxygen coverage reaches a new equilibrium, the adsorbed oxygen changes into a different species that can be employed in a dynamically modulated temperature measurement technique.

View Article Online
DOI: 10.1039/D5NA00783F

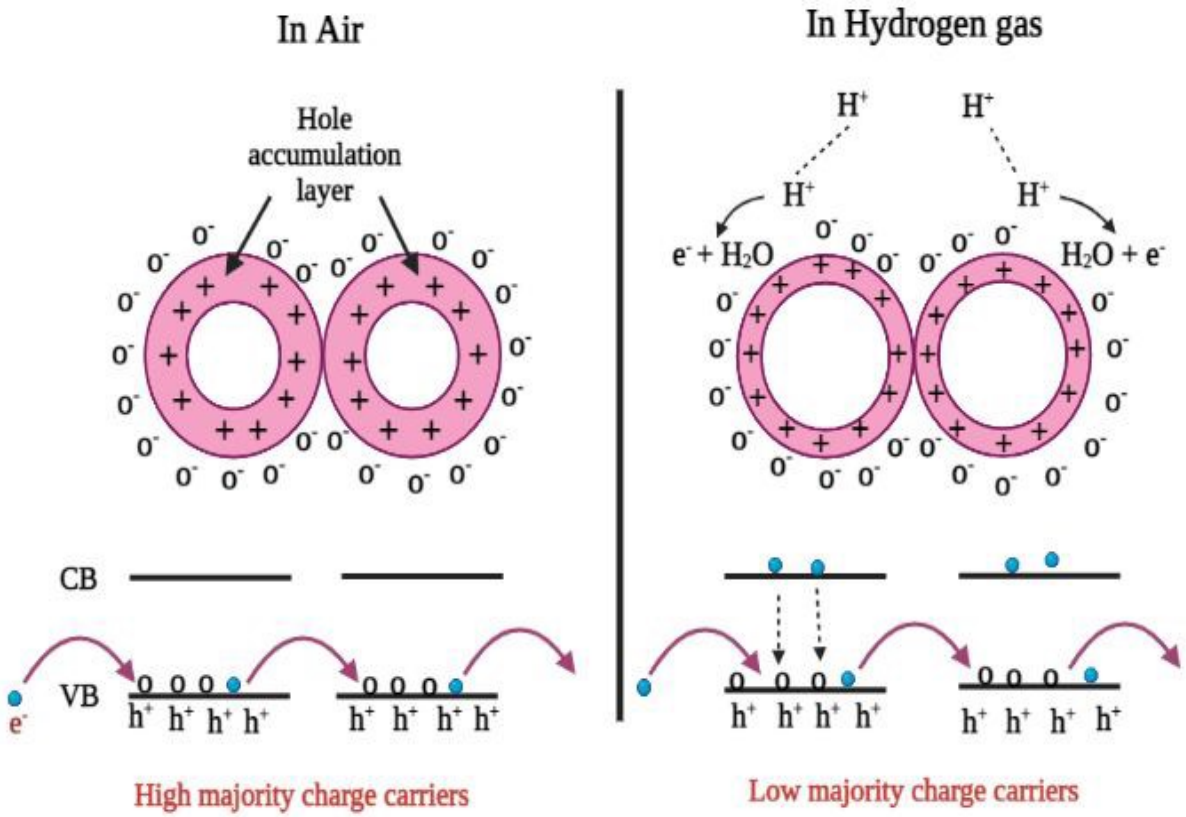

Fig. 13 Hydrogen sensing mechanism of SnO_2, Pani and SnO_2- Pani Nanocomposite (a) In presence of Air, (b) In presence of H_2

3.9. Electrochemical Studies

3.9.1. Cyclic Voltametry studies

The electrochemical behavior of the produced nano-crystalline electrode materials (SnO_2-PANI Nanocomposite) for electrochemical capacitors was examined using cyclic voltammetry (CV) in a 3 M KOH solution. The CV experiments were conducted at various scan rates (10, 20, 30, 40, 50, and 100 mV/s), and Figure 14 presents the results. A potential voltage range of 0.7 to 0.4 V vs. SCE was used for the CV tests. Cyclic voltammograms of all the samples were oval and rectangular in shape, suggesting that, as mentioned, a typical pseudocapacitve response takes

View Article Online
DOI: 10.1039/D5NA00783F

place at the graphite electrode/active material (SnO_2-PANI Nanocomposite)/electrolyte interface. These CV curves get better with increasing scan rates because they resemble pseudocapacitive nature [39]. Moreover, the current increases in proportion to the scan rate because at lower scan rates the electrolyte ions have more time to enter the material's pores; at higher scan rates, however, their current dependence on the scan rate limits their collection to the electrode's outermost surface. Equation (2) was utilized to calculate the values of specific capacitance.

Tab 3 displays the specific capacitance values computed for nanostructured SnO_2-PANI nanocomposite materials at various scan rates. At a scan rate of 10 mV/s, the SnO_2-PANI Nanocomposite demonstrated the highest specific capacitance (150.6Fg^{-1}) among the electrode materials.

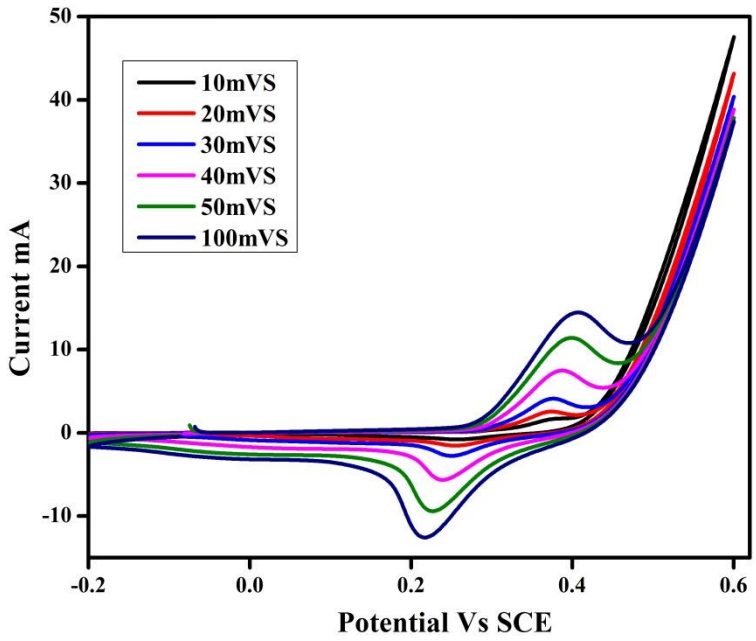

Fig. 14 Cyclic voltammogram obtained on SnO_2-PANI Nanocomposite nanostructured electrode materials at different scan rates in 3 M KOH electrolyte

Table 3 Specific capacitance data obtained on SnO_2-PANI Nanocomposite nanomaterials

View Article Online
DOI: 10.1039/D5NA00783F

SPECIFIC CAPACITANCE VALUES AT DIFFERENT SCAN RATES						
Electrode material	**100 mVs^{-1}**	**50 mVs^{-1}**	**40 mVs^{-1}**	**30 mVs^{-1}**	**20 mVs^{-1}**	**10 mVs^{-1}**
SnO_2-PANI Nanocomposite	100.53 Fg^{-1}	120.4 Fg^{-1}	140.6 Fg^{-1}	125.3 Fg^{-1}	134.94 Fg^{-1}	150.6Fg^{-1}

3.9.2. Galvanostatic charge discharge Studies

The electrochemical properties of electrode materials, like SnO_2-PANI Nanocomposite, were investigated through galvanostatic charge discharge (GCD) tests conducted in a 3 M KOH solution. The outcomes are shown in Figure 15. At current densities ranging from 1to 5 Ag^{-1}, the charge–discharge curves of electrode materials based on SnO_2-PANI nanocomposite were measured. Every GCD curve displayed a symmetrical triangle, suggesting that every sample exhibited optimal capacitor behavior[40].

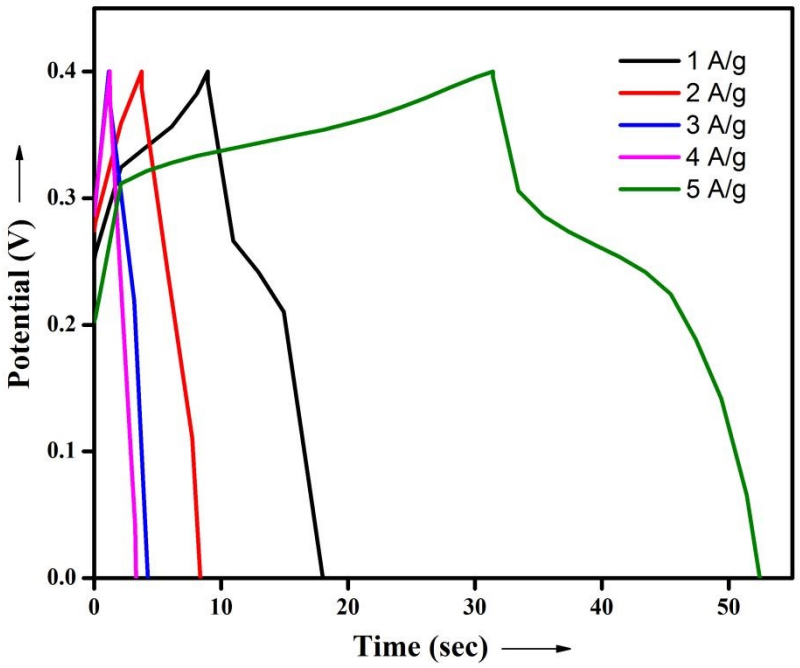

View Article Online
DOI: 10.1039/D5NA00783F

Fig. 15 Galvanostatic charge–discharge curves obtained on SnO_2-PANI Nanocomposite nanostructured electrode materials at different current densities

3.9.3. Impedance spectroscopy studies

The charge transport kinetics of the electrode materials were investigated using EIS measurements. According to reports, the Nyquist plot provides information on interfacial effects, electrode-electrolyte interactions, and equivalent series resistance (ESR). Using an amplitude of V, an EIS analysis of the SnO_2-PANI Nanocomposite electrode materials was conducted in the frequency range of 1 Hz to 1 kHz.

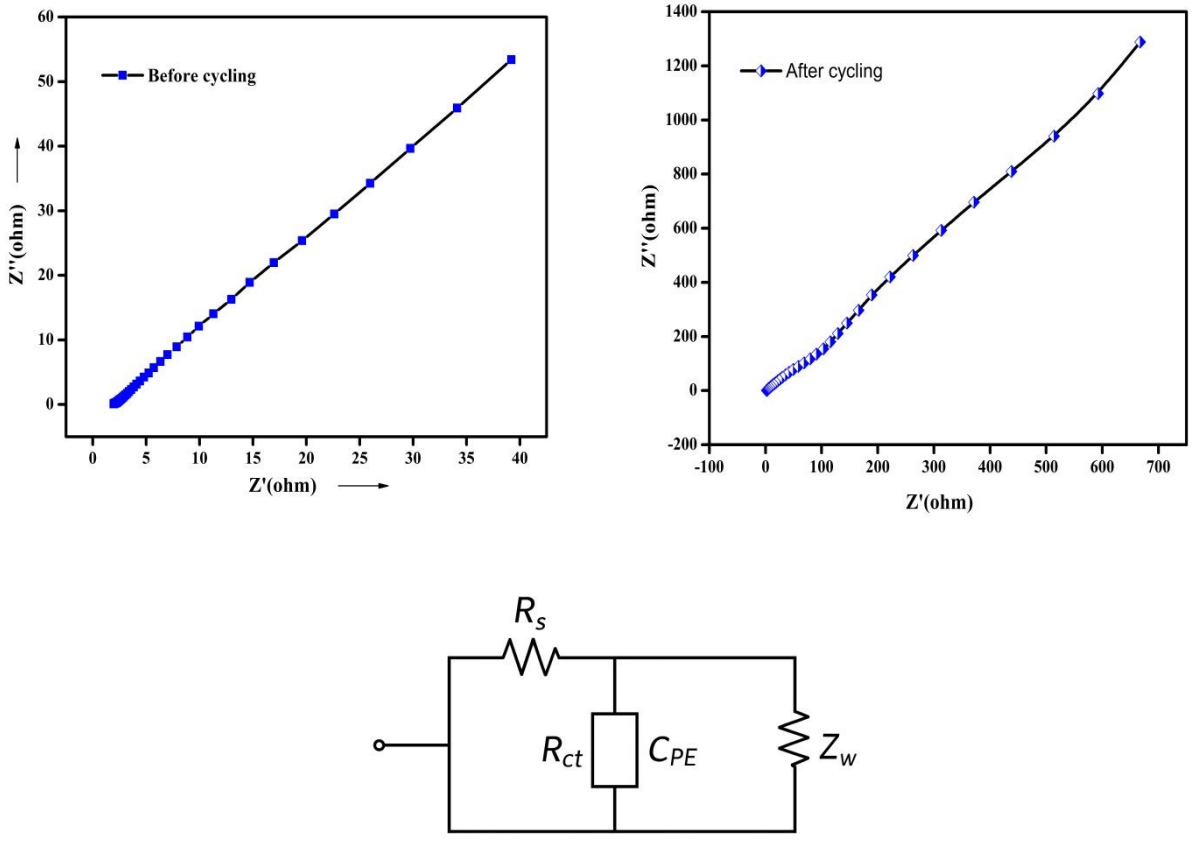

Fig. 16 Nyquist plots obtained on SnO_2-PANI Nanocomposite nanostructured electrode materials and Equivalent Circuit Diagram

View Article Online
DOI: 10.1039/D5NA00783F

The Nyquist plots generated on SnO_2-PANI Nanocomposite nanostructured electrode materials are displayed in Figure 16. Every Nyquist plot displayed a line that was almost exactly parallel to the fictitious components [41]. The described straight line obtained in the low frequency range indicates that all four samples exhibit perfect capacitance behavior. Moreover, a combination of electrode/electrolyte resistance, active material internal resistance, electrolyte interface resistance, and electrode/current collector contact resistance make up the EIS produced by the intercept at the actual impedance axis. The straight line slope of the low frequency area in the Nyquist plot corresponds to the Warburg behavior caused by rapid ion diffusion across the electrolyte/electrode interface. Consequently, we can say that supercapacitors can exhibit ideal blocking behavior at high frequencies and capacitive behavior at low frequencies [42]. It's feasible that this research will provide a clear process for creating electrode materials for high-performance supercapacitors based on SnO_2-PANI nanocomposite.

The EIS spectra of SnO_2, PANI, and SnO_2–PANI nanocomposites are shown in Figure 16, with the corresponding equivalent circuit inset. The semicircle observed at high frequency represents the charge transfer resistance (Rct), while the linear portion at low frequency corresponds to Warburg diffusion. The SnO_2–PANI composite exhibits a smaller Rct compared to pure SnO_2, indicating enhanced electron transfer due to the conductive PANI network. The slope of the low-frequency region suggests improved ionic diffusion, consistent with the porous morphology observed in SEM images. These results confirm that the composite structure facilitates both electronic and ionic transport, contributing to improved electrochemical performance.

3.10. Photocatalytic activity

View Article Online
DOI: 10.1039/D5NA00783F

Fig. 17 shows the photocatalytic degradation of the dye molecule rhodamine through chemically assisted synthesis. SnO_2-PANI nanocomposite are created at room temperature when exposed to 540 nm UV light. The Rhodamine dye molecule's decreasing level with longer UV exposure times indicates that the lowest peak, which was detected at 540 nm, represents the dye molecule's breakdown during UV irradiation [43].

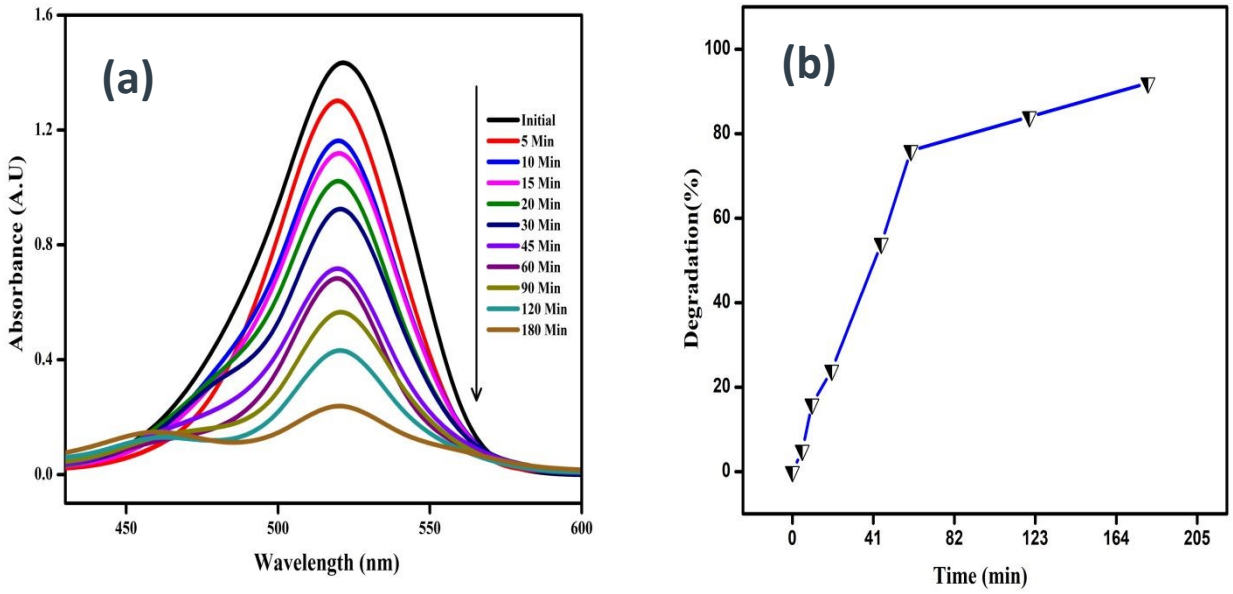

Fig. 17 Photocatalytic degradation of SnO_2-PANI Nanocomposite using Rhodamine dye (a) UV visible spectra (b) Percent Degradation

This shows that the semiconductor being excited by UV light to produce free radicals in the dye degradation process, where the excited electrons move from the valence band to the conduction band and generate high energy electron-hole pairs that transfer to adsorbed species on semiconductor results in heterogeneous photocatalysis, accounts for 92% of the degradation rate of the dye molecule using chemically created SnO_2-PANI Nanocomposite within 180 minutes[44]. After the photocatalytic activity was finished in three hours, rhodamine dye (0.2 L) was

View Article Online
DOI: 10.1039/D5NA00783F

successfully destroyed. It is worth mentioning that SnO_2-PANI Nanocomposite exhibits good performance as an adaptable photocatalytic nanoparticle.

3.10.1 Photocatalytic Charge Separation Mechanism

In SnO_2–PANI nanocomposites, the enhanced photocatalytic activity is primarily attributed to the **effective separation of photo-generated electron–hole pairs** facilitated by the synergistic interaction between SnO_2 and PANI:

1. Light Absorption and Excitation

Upon illumination, SnO_2 absorbs photons with energy ≥ bandgap (≈3.6 eV) to generate electron–hole pairs:

$$\mathbf{SnO_2 + h\nu \rightarrow e_{CB}^- + h_{VB}^+}$$

2. Charge Transfer at SnO_2–PANI Interface

Polyaniline (PANI), being a conductive polymer with delocalized π electrons, acts as an **electron acceptor or transporter**, facilitating the transfer of photo-generated electrons from SnO_2 to PANI.

This transfer suppresses electron–hole recombination, prolonging the lifetime of charge carriers.

3. Formation of Reactive Oxygen Species (ROS)

The transferred electrons on PANI reduce dissolved O_2 to superoxide radicals ($O_2^{\cdot-}$), while holes in SnO_2 oxidize water or OH^- to hydroxyl radicals ($OH^{\cdot}$):

$$\mathbf{e^- + O_2 \rightarrow O_2^{\cdot-}}$$

$$\mathbf{h^+ + H_2O \,/\, OH^- \rightarrow OH^{\cdot}}$$

These ROS species are responsible for the photocatalytic degradation of organic pollutants or microbial inactivation.

View Article Online
DOI: 10.1039/D5NA00783F

In summary, the SnO_2–PANI nanocomposite exhibits improved photocatalytic performance due to rapid electron transfer from SnO_2 to PANI, reduced recombination of electron–hole pairs, and increased generation of reactive oxygen species at the interface.

3.11. Toxicity study of Photocatalyst SnO_2-PANI Nanocomposite

The SnO_2-PANI Nanocomposite was shown to exhibit excellent toxicity on the eggs of adult zebra fish, as shown in Figure 18. After 48 hours of exposure, these adult zebrafish eggs demonstrated good hatching rate capabilities at concentrations of 100 and 200 µl, at the value of LC 50. Whenever the concentration of SnO_2-PANI Nanocomposite is increased, the degree of deformity also increases daily[45]. After 96 hours, the eggs' deformity reaches a high point at a concentration level of 200 µl. Comparable results are shown by the SnO_2-PANI Nanocomposite Mortality Rate, which shows that at a 200 µl concentration, high mortality happens at 96 hours, though eggs exposed to the control level also killed at 48 hours[46]. These variations make it very clear that the toxicity of nanocomposite depends on the particle's size, shape, capping agent, stability, and aquatic medium's quality in addition to the amount applied.

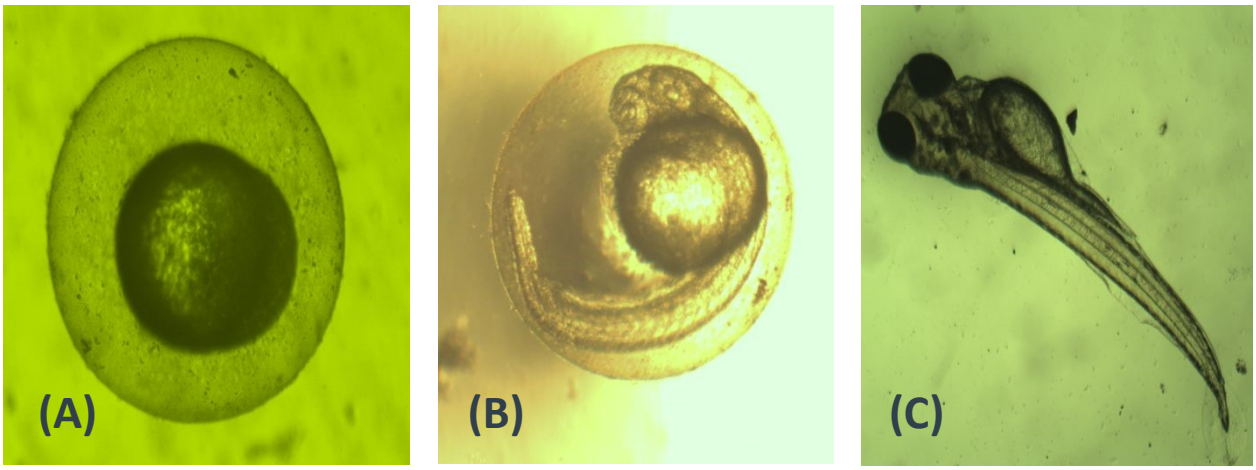

View Article Online
DOI: 10.1039/D5NA00783F

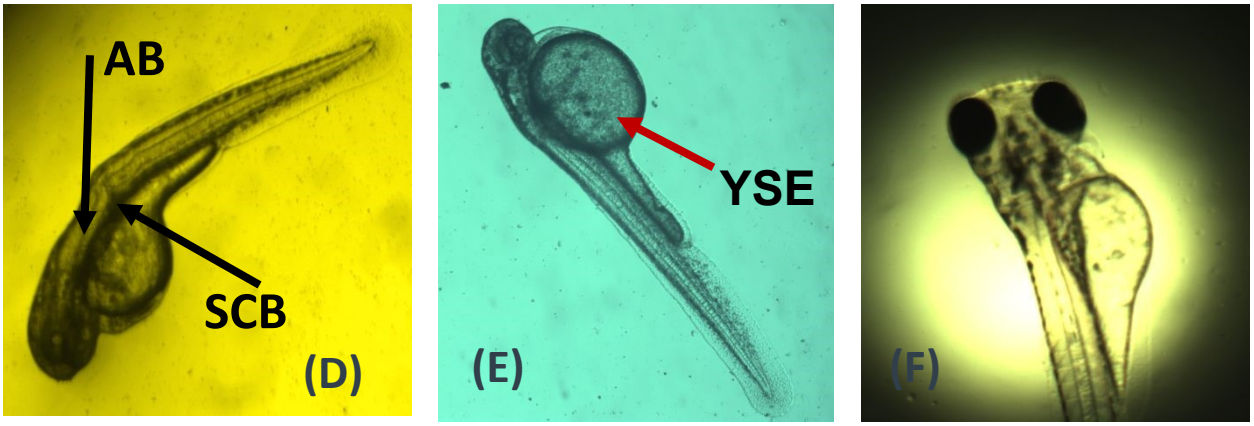

Fig. 18 SnO_2-PANI Nanocomposite imaging in zebrafish embryo and larva. A, B, C, D represents the control and Mortality image of SnO_2-PANI Nanocomposite, E and F represents Yolk Salk Edema (YSE) at 48 h, G represents Spinal Card Bend (SCB) and axis Bent (AB) at 72 h, H and I represents Tail Bent (TB), Head Malformation (HM) at 96 h.

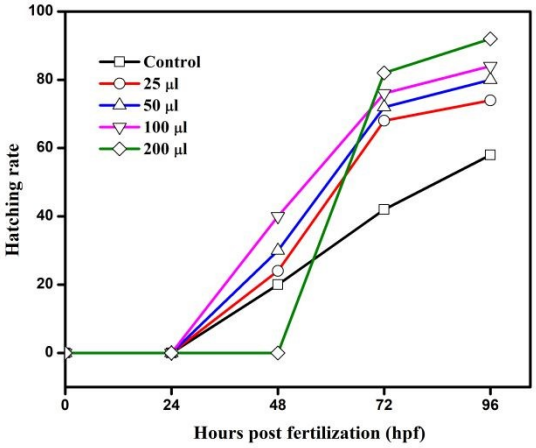

Hatching Rate

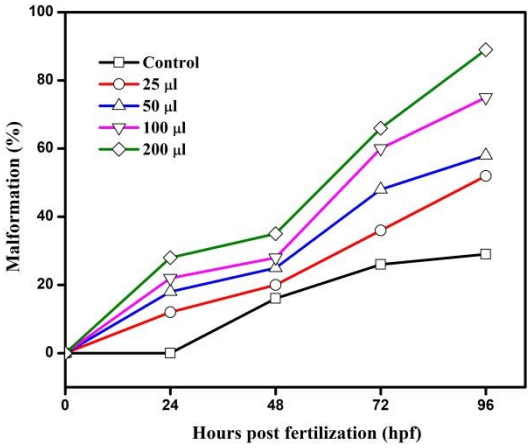

Malfotmation Rate

View Article Online
DOI: 10.1039/D5NA00783F

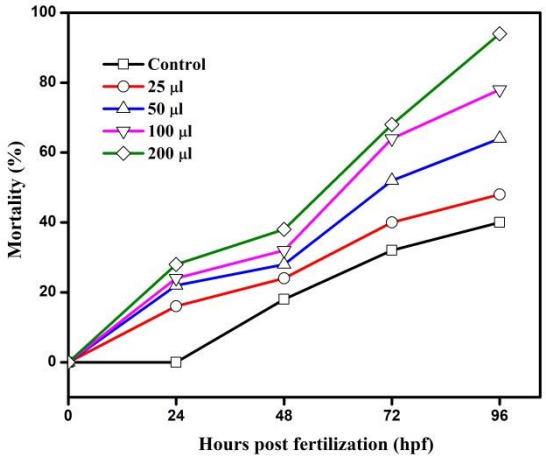

Mortality Rate

Fig. 19 Effects of SnO_2-PANI Nanocomposite on hatching rates, Malfotmation rates and Mortality rates of zebrafish embryos from 24-96 hpf.

3.12. Antibacterial activity

When the synthesized SnO_2-PANI Nanocomposite was tested against the bacterial strains Psedomonas, Enterobacter, and Staphylococcus aureus, inhibition zone values were obtained. The antibacterial activity of SnO_2-PANI Nanocomposite was assessed at different concentrations (10-100 µl); at all concentrations, 25 µl of the nanocomposite demonstrated antibacterial activity[47]. In the 10–20µl concentration range, no activity was seen. As a result, 25µl was chosen as the minimal inhibitory concentration (MIC). Table 4 and Figure 20 present the average values of the inhibition zone images and results, respectively.

View Article Online
DOI: 10.1039/D5NA00783F

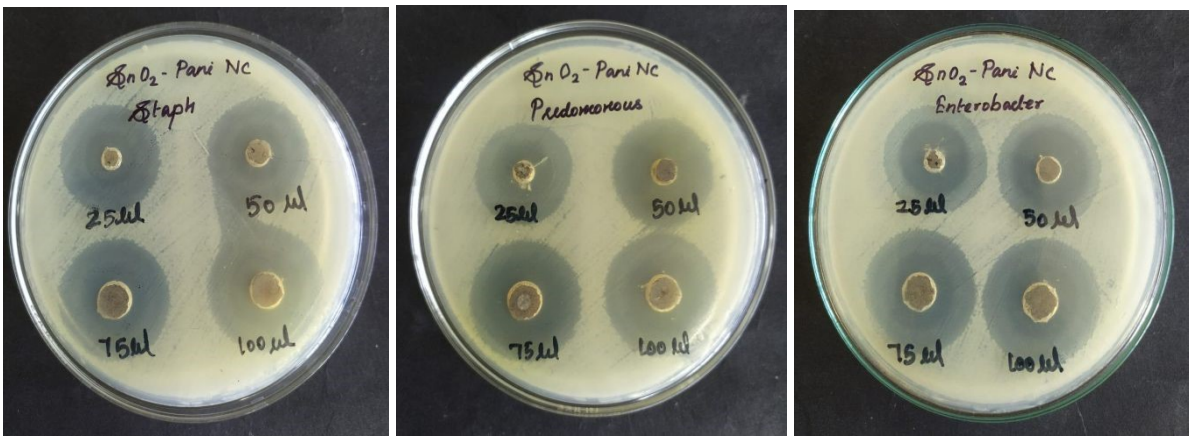

Fig. 20 Zone of inhibition of SnO_2-PANI Nanocomposite using various bacterial strains and standard antibiotic ciprofloxacin

The table displays the zone of inhibition for the SnO_2-PANI Nanocomposite and the common antibiotic Ciprofloxacin (C). The antibacterial activity of the SnO_2-PANI Nanocomposite suspension against both Gram-positive and Gram-negative bacteria was found to be high and comparable, as indicated by Table 4. Due to their size, SnO_2-PANI Nanocomposite can readily penetrate bacterial nuclei and exhibit a sizable and remarkable surface area where the greatest amount of contact with bacteria occurs[48]. This may be the cause of the best antibacterial activity of these SnO_2-PANI nanocomposite materials.

Table 4. Zone of inhibition of SnO_2-PANI Nanocomposite against selected bacterial Strains

Concentration	**Zone of Inhibition (cm in diameter)**		
	Enterobacter	***Staphylococcus aureus***	***Psedomonas***
	SnO_2-PANI Nanocomposite	**SnO_2-PANI Nanocomposite**	**SnO_2-PANI Nanocomposite**
25 µl	1.6	1.4	1.0
50 µl	1.8	1.6	1.2

View Article Online
DOI: 10.1039/D5NA00783F

75 µl	2.2	2.0	1.4
100 µl	2.4	2.5	1.8

Table: 5 Comparative Summary Table

Study	Synthesis Method	Application & Key Performance / Observation	Remarks / Limitations	Reference
SnO_2-PANI/Pd nanocomposite (nanosheets + PANI doped with Pd)	Hydrothermal SnO_2 → combine with PANI + Pd (likely in situ polymerization)	Hydrogen (H_2) sensing at room temperature (50–400 ppm) — enhanced sensitivity vs individual components	Good proof-of-concept; but uses Pd (noble metal) — increases cost. No long-term stability / cycle tests reported.	6
Ag-SnO_2 / PANI composite nanofibers	Electrospinning + calcination for Ag–SnO_2; dip-coating PANI by in situ polymerization	Hydrogen sensing — sensitive at ≈ 42 °C (much lower than bare SnO_2)	Demonstrates low-temperature operation; but required Ag doping. No report on selectivity, cross-gas interference, long-term cycling.	49
SnO_2 / PANI electrospun nanofibers (no catalytic dopants)	Electrospinning composite fibers; characterized by XRD, SEM/EDX, UV-vis; tested for H_2 & CO sensing at ~ 35 °C; fast response/recovery (<30 s)	Gas sensing (H_2, CO) — promising sensitivity and response kinetics at low temperature	Encouraging for low-cost sensors; but sensitivity vs concentration curve, long-term stability, reproducibility over many cycles not fully explored.	7
SnO_2/PANI nanoparticles (hydrothermal + PANI adsorption) for Cr(VI) reduction under visible	Hydrothermal SnO_2; PANI adsorption in DMF; composite dried and characterized (XRD, XPS, TEM, UV-vis DRS, EIS)	Photocatalytic reduction of Cr(VI) under visible light — up to 23× rate compared to bare SnO_2	Demonstrates visible-light-driven photocatalysis via p–n heterojunction; but only Cr(VI) reduction tested;	50

View Article Online
DOI: 10.1039/D5NA00783F

light			limited data on reusability, stability, and extension to other pollutants/dyes.	
SnO_2/PANI nanocomposites (general) — review of photocatalytic behavior	Analysis of prior works showing that coupling PANI (p-type) with SnO_2 (n-type) improves visible-light absorption and charge separation — enhancing photocatalytic activity compared to SnO_2 alone	Photocatalysis (dyes, pollutants) — better performance vs bare SnO_2; more environmentally friendly by-product profile	Encouraging rationale; but detailed experimental parameters vary widely; systematic comparison lacking.	[51]
SnO_2-based (not necessarily PANI) composites for antibacterial and multifunctional uses	Many studies show SnO_2 NPs or doped SnO_2 have antibacterial activity (Gram +/−) via ROS generation, often light-activated	Antibacterial / antimicrobial potential; sometimes combined with photocatalysis or energy storage (in other composites)	But for SnO_2–PANI specifically, antibacterial action remains almost unexplored. Recent 2025 work reports synthesis but does not (yet) report biological results.	[52]

4. CONCLUSION

In this present research binary nanocomposite were prepared using such as polymer (Polyaniline) and SnO to form (SnO_2-PANI NCs). The synthesized nanocomposite were characterized using various techniques like UV-Vis Spectroscopy, X-Ray Diffraction, Fourier Transform Infra-Red Spectroscopy, Particle Size Analysis, Scanning Electron Microscope, Elemental Analysis, Thermo Gravimetric Analysis and Atomic Force Microscopy. The nanocomposite were involved in various studies like Gas sensing, Electrochemical, Supercapacitor, Photocatalyst, Antibacterial and toxicity studies.

View Article Online
DOI: 10.1039/D5NA00783F

The UV band gap study revealed that the band gap energy of PANI-SnO nanoparticle is about 2.3eV. The FTIR study showed that the functional moieties that are involved in the nanoparticle synthesis and the presence of nanoparticle peaks in the solution. The particle size analysis showed that the particles are in the range of 70-110 nm size. The SEM-EDAX analysis depicted the particles are mostly spherical and agglomerated and the EDAX showed the presence of Sn in the nanoparticle solution with strong band at 3.5 KeV. The gas sensing property of the nanoparticle showed good sensitivity for CO_2 at 50 ppm. The electrode material is highly sensitive to H_2 when compared to other gases like O_2, CO_2, NH_3, and LPG. The electrode material is stable for 50 days with 94% sensing capacity. The electrochemical study showed that the particles have high current density and specific surface area. The bimetallic nanoparticle was used to degrade the Rhodamine dye in a photocatalytic chamber. The nanoparticles removed 92% dye in 180 min with higher removal efficiency. The toxicity test was performed to test the toxic nature of the photocatalyst and the nanoparticles showed mild toxicity to the model animal. The antibacterial test was conducted for Gram positive and negative bacteria and the particles showed good activity when compared to the control.

Author contributions

Dr. E. Amutha – Writing and review, Manuscript preparation and revision, Methodology, Validation, Conceptualization, Investigation; Dr. S. Rajaduraipandian - Implementation of experiments, Data collection, Sample Analysis, writing and review; T. Madhumitha – Software, Data collection; G. Annadurai - Supervision, Investigation, Implementation of experiments and Manuscript revision; Vijayalakshmi Shankar - Implementation of experiments, Validation and review.

Acknowledgments

View Article Online
DOI: 10.1039/D5NA00783F

The authors would like to express their gratitude to the Sri Paramakalyani Centre of Excellence in Environmental Sciences at Manonmaniam Sundaranar University, Alwarkurichi for their technical and financial support. Special thanks to Archbishop Casimir Instrumentation Center (ACIC) (Instrumental Analysis), and Kalasalingam University (X-ray Diffraction and Microscopy Analysis) for their technical assistance. Dr. E. Amutha acknowledges the Council of Scientific & Industrial Research (CSIR), India, for the support provided through File No. 09/0652(19575)/2024-EMR-I.

DECLARATIONS

Funding: This research work was supported by the Anusandhan National Research Foundation (ANRF) under the Partnerships for Accelerated Innovation and Research (PAIR) project, Government of India, sanction order ANRF/PAIR/2025/000011/PAIR-B

Conflict of Interest: The authors declare that there is no conflict of interest

Data availability: The datasets used and/or analyzed during the current study are available from the corresponding author on reasonable request.

References

1 Q. M. Al-Bataineh, M. Telfah, R. Abu-Zurayk, A. Benchaabane, C. J. Tavares and A. Telfah, Nano-SnO2/polyaniline composite films for surface plasmon resonance, *Materials Chemistry and Physics*, 2023, **293**, 126816.

2 M. Kandasamy, A. Seetharaman, I. M. Babu, J. J. William, G. Muralidharan, D. Sivasubramanian, K. Jothivenkatachalam, M. Imran and B. Chakraborty, Experimental and theoretical investigations of a multiwalled carbon nanotubes/SnO2/polyaniline ternary nanohybrid electrode for energy storage, *Surfaces and Interfaces*, 2022, **30**, 101978.

3 A. Singh and B. C. Yadav, Photo-responsive highly sensitive CO2 gas sensor based on SnO2@CdO heterostructures with DFT calculations, *Surfaces and Interfaces*, 2022, **34**, 102368.

View Article Online
DOI: 10.1039/D5NA00783F

4 S. Singh, N. Verma, A. Singh and B. C. Yadav, Synthesis and characterization of CuO–SnO2 nanocomposite and its application as liquefied petroleum gas sensor, *Materials Science in Semiconductor Processing*, 2014, **18**, 88–96.

5 Z. Luo, Y. Zhu, E. Liu, T. Hu, Z. Li, T. Liu and L. Song, Synthesis of polyaniline/SnO2 nanocomposite and its improved electrochemical performance, *Materials Research Bulletin*, 2014, **60**, 105–110.

6 R. K. Pippara, P. S. Chauhan, A. Yadav, V. Kishnani and A. Gupta, Room temperature hydrogen sensing with polyaniline/SnO2/Pd nanocomposites, *Micro and Nano Engineering*, 2021, **12**, 100086.

7 H. J. Sharma, M. A. Salorkar and S. B. Kondawar, H2 and CO gas sensor from SnO2/polyaniline composite nanofibers fabricated by electrospinning, *Advanced Materials Proceedings*, 2017, **2**, 61–66.

8 S. Krithika and J. Balavijayalakshmi, Investigation of structural, morphological and electrochemical properties of MoS2/PANI/SnO2 nanocomposites for energy storage applications, *Inorganic Chemistry Communications*, 2023, **148**, 110324.

9 A. R. Athira, T. Merin, K. Anupama, K. A. Ann Mary and T. S. Xavier, Surfactant incorporated polyaniline/Co3O4/rGO ternary hybrid composite symmetric supercapacitors for efficient energy storage applications, *Diamond and Related Materials*, 2022, **130**, 109475.

10 Y. V. Naik, M. Y. Kariduraganavar, H. T. Srinivasa and P. B. Siddagangaiah, High surface wetting and conducting NiO/PANI nanocomposites as efficient electrode materials for supercapacitors, *Inorganic Chemistry Communications*, 2022, **138**, 109275.

11 A. Baby, J. Vigneshwaran, P. B. Sreeja and S. P. Jose, in *Handbook of Energy Materials*, ed. R. Gupta, Springer Nature, Singapore, 2022, pp. 1–28.

12 N. T. To, D. V. Lai, N. T.-M. Quan, X. T. Chu, L. T. T. Dang, H. M. Chu, D. V. Nguyen and D. H. Nguyen, Novel Synthesis of Pani/Zno Nanohybrid for Enhanced No2 Gas Sensing Performance at Low Temperatures, 2022, preprint, 4064417, DOI: 10.2139/ssrn.4064417.

13 J. Kharbanda and R. Priya, Synthesis and applications of tin oxide nanoparticles: An overview, *Materials Today: Proceedings*, 2022, **68**, 916–921.

14 P. Kaushik, R. Bharti, R. Sharma, M. Verma, R. T. Olsson and A. Pandey, Progress in synthesis and applications of Polyaniline-Coated Nanocomposites: A comprehensive review, *European Polymer Journal*, 2024, **221**, 113574.

15 V. Eskizeybek, F. Sarı, H. Gülce, A. Gülce and A. Avcı, Preparation of the new polyaniline/ZnO nanocomposite and its photocatalytic activity for degradation of methylene blue and malachite

View Article Online
DOI: 10.1039/D5NA00783F

green dyes under UV and natural sun lights irradiations, *Applied Catalysis B: Environmental*, 2012, **119–120**, 197.

16 C. Messaadi, T. Ghrib, J. Jalali, M. Ghrib, A. Alyami, M. Gaidi, M. Manso-Silván and H. Ezzaouia, Synthesis and Characterization of SnO2-TiO2 Nanocomposites Photocatalysts, *Current Nanoscience*, DOI:10.2174/1573413714666180927110912.

17 M. Ben Ali, F. Barka-Bouaifel, B. Sieber, H. Elhouichet, A. Addad, L. Boussekey, M. Férid and R. Boukherroub, Preparation and characterization of Ni-doped ZnO–SnO2 nanocomposites: Application in photocatalysis, *Superlattices and Microstructures*, 2016, **91**, 225–237.

18 L. U. Okafor, O. A. Amaechi, O. O. Kingsley and C. P. Odeh, Synthesis and Structural Characterization of Polyaniline–Tin-Oxide Nanocomposite for Device Application, *Unizik Journal of Technology, Production and Mechanical Systems*, 2025, **7**, 344–350.

19 Q. M. Al-Bataineh, A. B. Migdadi, A. Telfah, A. A. Ahmad, A. M. Alsaad and C. J. Tavares, Physical and chemical characterization of polyaniline (PANI)/indium tin oxide nanoparticles (ITONPs) nanocomposite films, *Materials Chemistry and Physics*, 2022, **290**, 126387.

20 P. Wei, H. Xiaowei and C. Yan, Preparation and Characterization of Poly (vinyl alcohol)/Antimony-Doped Tin Oxide Nanocomposites, *International Journal of Polymeric Materials and Polymeric Biomaterials*, 2010, **60**, 223–232.

21 A. L. C. Silva, J. C. Ugucioni, S. Correa, J. D. Ardisson, W. A. A. Macedo, J. P. Silva, A. A. C. Cotta and A. D. B. Brito, Synthesis and characterization of nanocomposites consisting of polyaniline, chitosan and tin dioxide, *Materials Chemistry and Physics*, 2018, **216**, 402–412.

22 H. N. Lim, R. Nurzulaikha, I. Harrison, S. S. Lim, W. T. Tan, M. C. Yeo, M. A. Yarmo and N. M. Huang, Preparation and characterization of tin oxide, SnO2 nanoparticles decorated graphene, *Ceramics International*, 2012, **38**, 4209–4216.

23 S. G. Pawar, M. A. Chougule, S. L. Patil, B. T. Raut, P. R. Godse, S. Sen and V. B. Patil, Room Temperature Ammonia Gas Sensor Based on Polyaniline-TiO_2 Nanocomposite, *IEEE Sensors Journal*, 2011, **11**, 3417–3423.

24 S. Kanimozhi, S. Suresh, S. Thambidurai, N. Suresh and K. M. Prabu, Facile co-precipitation assisted synthesis and characterization of zinc oxide-tin oxide nanocomposites and their performance evaluation as photoanodes in dye-sensitized solar cell, *Results in Chemistry*, 2022, **4**, 100615.

25 P. Manivel, S. Ramakrishnan, N. K. Kothurkar, A. Balamurugan, N. Ponpandian, D. Mangalaraj and C. Viswanathan, Optical and electrochemical studies of polyaniline/SnO2 fibrous nanocomposites, *Materials Research Bulletin*, 2013, **48**, 640–645.

View Article Online
DOI: 10.1039/D5NA00783F

26 C. Reddy and R. Holze, Synthesis and characterization of a polyaniline-modified SnO2 nanocomposite, *Ionics*, DOI:10.1007/s11581-011-0648-x.

27 S. G. Pawar, S. L. Patil, M. A. Chougule, A. T. Mane, D. M. Jundale and V. B. Patil, Synthesis and Characterization of Polyaniline:TiO2 Nanocomposites, *International Journal of Polymeric Materials and Polymeric Biomaterials*, 2010, **59**, 777–785.

28 H. Tai, Y. Jiang, G. Xie, J. Yu and X. Chen, Fabrication and gas sensitivity of polyaniline–titanium dioxide nanocomposite thin film, *Sensors and Actuators B: Chemical*, 2007, **125**, 644–650.

29 D. C. Schnitzler, M. S. Meruvia, I. A. Hümmelgen and A. J. G. Zarbin, Preparation and Characterization of Novel Hybrid Materials Formed from (Ti,Sn)O2 Nanoparticles and Polyaniline, *Chem. Mater.*, 2003, **15**, 4658–4665.

30 F. Caputo, J. Clogston, L. Calzolai, M. Roesslein and A. Prina-Mello, Measuring particle size distribution of nanoparticle enabled medicinal products, the joint view of EUNCL and NCI-NCL. A step by step approach combining orthogonal measurements with increasing complexity, *Journal of Controlled Release*, DOI:10.1016/j.jconrel.2019.02.030.

31 P. Klapetek, M. Valtr, D. Nečas, O. Salyk and P. Dzik, Atomic force microscopy analysis of nanoparticles in non-ideal conditions, *Nanoscale Res Lett*, 2011, **6**, 514.

32 J. Chauhan, Preparation and Characterization of Polyaniline/ZnO Composite Sensor, *Journal of Nanomedicine Research*, DOI:10.15406/jnmr.2017.05.00104.

33 T. Krishnakumar, R. Jayaprakash, T. Prakash, D. Sathyaraj, N. Donato, S. Licoccia, M. Latino, A. Stassi and G. Neri, CdO-based nanostructures as novel CO2gas sensors, *Nanotechnology*, 2011, **22**, 325501.

34 M. A. Farea, G. B. Bhanuse, H. Y. Mohammed, M. O. Farea, M. Sallam, S. M. Shirsat, M.-L. Tsai and M. D. Shirsat, Ultrahigh sensitive and selective room-temperature carbon monoxide gas sensor based on polypyrrole/titanium dioxide nanocomposite, *Journal of Alloys and Compounds*, 2022, **917**, 165397.

35 C.-H. Hsieh, L.-H. Xu, J.-M. Wang and T.-M. Wu, Fabrication of polypyrrole/tin oxide/graphene nanoribbon ternary nanocomposite and its high-performance ammonia gas sensing at room temperature, *Materials Science and Engineering: B*, 2021, **272**, 115317.

36 D. Matatagui, J. López-Sánchez, A. Peña, A. Serrano, A. del Campo, O. R. de la Fuente, N. Carmona, E. Navarro, P. Marín and M. del Carmen Horrillo, Ultrasensitive NO2 gas sensor with insignificant NH3-interference based on a few-layered mesoporous graphene, *Sensors and Actuators B: Chemical*, 2021, **335**, 129657.

View Article Online
DOI: 10.1039/D5NA00783F

37 S. Kafash and H. Milani Moghaddam, Porous polyaniline tube-like/TiO2 nano-heterostructure for sensing hydrogen gas at environmental conditions, *International Journal of Hydrogen Energy*, 2022, **47**, 14740–14758.

38 A. Umar, A. A. Ibrahim, H. Algadi, H. Albargi, M. A. Alsairi, Y. Wang and S. Akbar, Enhanced NO2 gas sensor device based on supramolecularly assembled polyaniline/silver oxide/graphene oxide composites, *Ceramics International*, 2021, **47**, 25696–25707.

39 D. Yang, in *Nanocomposites - New Trends Dev*, 2012.

40 M. Ates, I. Mizrak, O. Kuzgun and S. Aktas, Synthesis, characterization, and supercapacitor performances of activated and inactivated rGO/MnO2 and rGO/MnO2/PPy nanocomposites, *Ionics*, 2020, **26**, 4723–4735.

41 M. S. Yadav and S. K. Tripathi, Synthesis and characterization of nanocomposite NiO/activated charcoal electrodes for supercapacitor application, *Ionics*, 2017, **23**, 2919–2930.

42 M. Naveed ur Rehman, T. Munawar, M. S. Nadeem, F. Mukhtar, A. Maqbool, M. Riaz, S. Manzoor, M. N. Ashiq and F. Iqbal, Facile synthesis and characterization of conducting polymer-metal oxide based core-shell PANI-Pr2O–NiO–Co3O4 nanocomposite: As electrode material for supercapacitor, *Ceramics International*, 2021, **47**, 18497–18509.

43 K. Selvam, C. Sudhakar, T. Selvankumar, B. Senthilkumar, W. Kim, M. M. Al-Ansari and L. Al-Humaid, Photocatalytic degradation of malachite green and antibacterial potential of biomimetic-synthesized zirconium oxide nanoparticles using Annona reticulata leaf extract, *Appl Nanosci*, DOI:10.1007/s13204-021-02148-0.

44 K. Chand, D. Cao, D. Eldin Fouad, A. Hussain Shah, A. Qadeer Dayo, K. Zhu, M. Nazim Lakhan, G. Mehdi and S. Dong, Green synthesis, characterization and photocatalytic application of silver nanoparticles synthesized by various plant extracts, *Arabian Journal of Chemistry*, 2020, **13**, 8248–8261.

45 Y.-L. Hu, W. Qi, F. Han, J.-Z. Shao and J.-Q. Gao, Toxicity evaluation of biodegradable chitosan nanoparticles using a zebrafish embryo model, *Int J Nanomedicine*, 2011, **6**, 3351–3359.

46 A. Guillén, Y. Ardila, M. J. Noguera, A. L. Campaña, M. Bejarano, V. Akle and J. F. Osma, Toxicity of Modified Magnetite-Based Nanocomposites Used for Wastewater Treatment and Evaluated on Zebrafish (Danio rerio) Model, *Nanomaterials*, 2022, **12**, 489.

47 N. Liu, X. G. Chen, H. J. Park, C. G. Liu, C. S. Liu, X. H. Meng and L. J. Yu, Effect of MW and concentration of chitosan on antibacterial activity of Escherichia coli, *Carbohydrate polymers*, 2006, **64**, 60–65.

View Article Online
DOI: 10.1039/D5NA00783F

48 G. Das, J. K. Patra and H.-S. Shin, Biosynthesis, and potential effect of fern mediated biocompatible silver nanoparticles by cytotoxicity, antidiabetic, antioxidant and antibacterial, studies, *Materials Science and Engineering: C*, 2020, **114**, 111011.

49 S. B. Kondawar, A. M. More, H. J. Sharma and S. P. Dongre, Ag-SnO2/Polyaniline composite nanofibers for low operating temperature hydrogen gas sensor, *Materials NanoScience*, 2017, **4**, 13–18.

50 Polyaniline modified SnO 2 nanoparticles for efficient photocatalytic reduction of aqueous Cr(VI) under visible light | Request PDF, *ResearchGate*, DOI:10.1016/j.seppur.2018.03.010.

51 U. Rajaji, S. Eva Gnana Dhana Rani, S.-M. Chen, K. Rajakumar, M. Govindasamy, F. M. Alzahrani, N. S. Alsaiari, M. Ouladsmane and I. Sharmila Lydia, Synergistic photocatalytic activity of SnO2/PANI nanocomposite for the removal of direct blue 15 under UV light irradiation, *Ceramics International*, 2021, **47**, 29225–29231.

52 J. S. Algethami, M. S. Hassan, T. Amna, F. A. Sheikh, M. A. M. Alhamami, A. F. Seliem, M. Faisal and H. Y. Kim, Nanotextured CeO2–SnO2 Composite: Efficient Photocatalytic, Antibacterial, and Energy Storage Fibers, *Nanomaterials*, 2023, **13**, 1001.

View Article Online
DOI: 10.1039/D5NA00783F

Data availability: The datasets used and/or analyzed during the current study are available from the corresponding author on reasonable request.